Univerza
v Ljubljani

Fakulteta
*za gradbeništvo
in geodezijo*

Jamova 2
1000 Ljubljana, Slovenija
http://www3.fgg.uni-lj.si/

DRUGG – Digitalni repozitorij UL FGG
http://drugg.fgg.uni-lj.si/

Ta članek je avtorjeva zadnja recenzirana različica, kot je bila sprejeta po opravljeni recenziji.

Prosimo, da se pri navajanju sklicujte na bibliografske podatke, kot je navedeno:

University
of Ljubljana

Faculty of
*Civil and Geodetic
Engineering*

Jamova 2
SI – 1000 Ljubljana, Slovenia
http://www3.fgg.uni-lj.si/

DRUGG – The Digital Repository
http://drugg.fgg.uni-lj.si/

This version of the article is author's manuscript as accepted for publishing after the review process.

When citing, please refer to the publisher's bibliographic information as follows:

Quadrilateral finite element with embedded strong discontinuity for failure analysis of solids

Jaka Dujc[1,2], Boštjan Brank[1,*], Adnan Ibrahimbegovic[2]
[1]University of Ljubljana,
Faculty of Civil and Geodetic Engineering, Ljubljana, Slovenia
[2]Ecole Normale Supérieure de Cachan, Cachan, France
[*]corresponding author, E-mail: bbrank@fgg.uni-lj.si, fax:+386 1 425 06 93

Abstract

We present a quadrilateral finite element with discontinuous displacement fields that can be used to model material failure in 2d brittle and ductile solids. The element provides mesh-objective results. The element's kinematics can represent linear displacement jumps along the discontinuity line in both normal and tangential directions to the line. The cohesive law in the discontinuity line is based on rigid-plasticity model with softening. The material of the bulk of the element is described by hardening plasticity model. Static condensation of the jump-in-displacements kinematic parameters is made, which provides standard form of the element stiffness matrix. However, in order to make the discontinuity growth algorithm more robust, the continuity of the failure line between the elements is enforced. Several numerical tests show that the element can describe constant and linear separation modes without spurious transfer of the stresses. Other numerical examples represent failure of pure concrete, composite and metal 2d solids.

Keywords: embedded discontinuity, quadrilateral finite element, material failure, softening

1 Introduction

Finite element analysis of structures, whose material response is characterized by softening phenomena, such as cracking (in concrete and masonry) or shear bands (in metals and soils), is a nontrivial task. It is well known that the standard finite element models of solids and structures lead to lack of invariance of the computed numerical solution with respect to the mesh for stress-strain relationships with strain-softening. This is due to the fact that the underlying mathematical model, i.e. boundary value problem, is ill-posed and uniqueness of the solution is lost. In the limiting case of very fine mesh, a material failure without any dissipation is obtained by the finite element analysis, which is physically impossible, see e.g. [13] . Different approaches have been proposed to overcome these mathematical, physical and numerical deficiencies of the standard finite element models of

1

solids and structures to solve structural problems involving strain-softening. For recent review see e.g. [1].

In recent years, finite element formulations based on discontinuous displacement fields have become very popular solution for the above mentioned deficiencies, see e.g. [14], [9]. The incorporation of strong discontinuities into a continuous displacements is related to cohesive-zone models. There, the softening is controlled by an evolution law for the normal traction at the crack surface in terms of the crack width. The crack width represents a displacement jump at the crack surface. When applying such a model to the finite element analysis of material failure, mesh-independent results are obtained. The implementation of displacement jumps into finite element models can be achieved by different concepts. One of the concepts is to embedded the displacement jumps within a finite element. Several frameworks can be used for this purpose. We show in this paper that the convenient framework to embed displacement jumps into the standard finite element is the incompatible mode method, see e.g. [15].

In this work we present a detailed derivation of a plane stress quadrilateral finite element with embedded strong discontinuity in displacements. Its kinematics can model linear jumps in both normal and tangential displacements along the discontinuity line. Special attention is given to proper description of element separation modes without spurious transfer of the stresses across the discontinuity line. It is shown that this can be effectively accomplished in the framework of the incompatible mode method. The element can represent elasto-plastic material response, which includes hardening plasticity for the bulk and softening plasticity at the discontinuity line. The latter is controlled by evolution laws for tractions in terms of displacement jumps. The derived element is a refinement with respect to the constant strain triangle that has been used in vast majority of works related to embedded discontinuity finite element modeling of failure in 2d solids, e.g. [2], [16], [14], [10] and goes in line with the recent developments presented in [8] and [11]. In order to keep the standard form of the element stiffness matrix, static condensation of jump-in-displacement parameters is performed. Moreover, in order to make the discontinuity growth algorithm more robust, the continuity of the failure line between the elements is enforced.

The paper is organized as follows. In section 2 the element is derived, in section 3 the computational issues are addressed in detail, in section 4 numerical examples are presented, and in section 5 conclusions are drawn.

2 An embedded discontinuity quadrilateral element for planar problems

In this section we present a two-dimensional quadrilateral element with embedded strong discontinuity in displacements. The element can represent elasto-plastic material response that includes localized material failure described by softening plasticity.

2.1 Kinematic equations

2.1.1 Displacements

We consider a 4-node quadrilateral finite element occupying domain $\Omega^e \subset \mathbb{R}^2$ (Figure 1). The element may be divided by a line Γ^e into two subdomains: Ω^{e+} and Ω^{e-} ($\Omega^e = \Omega^{e+} \cup \Omega^{e-}$). Element's geometry is defined by the bilinear mapping $\boldsymbol{\xi} \mapsto \boldsymbol{x}^h$ ($\boldsymbol{\xi} \in [-1,1] \times [-1,1]$; $\boldsymbol{x}^h \in \Omega^e$), with

$$\boldsymbol{x}^h\left(\boldsymbol{\xi}\right)|_{\Omega^e} = \sum_{a=1}^{4} N_a\left(\boldsymbol{\xi}\right)\boldsymbol{x}_a; \qquad \boldsymbol{x}_a = [x_a, y_a]^T; \qquad \boldsymbol{\xi} = [\xi, \eta]^T, \qquad (1)$$

where $\boldsymbol{x}_a$ are coordinates of the finite element node a, and

$$N_a\left(\boldsymbol{\xi}\right) = \frac{1}{4}\left(1 + \xi_a\xi\right)\left(1 + \eta_a\eta\right); \qquad \begin{array}{c|cccc} a & 1 & 2 & 3 & 4 \\ \hline \xi_a & -1 & 1 & 1 & -1 \\ \hline \eta_a & -1 & -1 & 1 & 1 \end{array} . \qquad (2)$$

The superscript h denotes an approximation. Element's displacement field is defined by nodal displacements and jump-in-displacement parameters. The latter are associated with the line Γ^e, which will be further called the discontinuity line. Nodal displacements in x and y directions of the node a are denoted as u_{xa} and u_{ya}, Figure 1. To describe strong discontinuity in displacements, additional degrees of freedom are introduced: parameters α_{n0} and α_{n1} define the displacement jump in direction of unit vector $\boldsymbol{n}$, and parameters α_{m0} and α_{m1} define the displacement jump in direction of unit vector $\boldsymbol{m}$, Figure 1. We approximate the element's displacement field as:

$$\boldsymbol{u}^h(\boldsymbol{\xi}, \Gamma^e)|_{\Omega^e} = [u_x^h, u_y^h]^T = \underbrace{\sum_{a=1}^{4} N_a(\boldsymbol{\xi})\boldsymbol{d}_a}_{\boldsymbol{u}_d^h} +$$

$$+ \underbrace{\boldsymbol{p}_{n0}(\boldsymbol{\xi}, \Gamma^e)\alpha_{n0} + \boldsymbol{p}_{n1}(\boldsymbol{\xi}, \Gamma^e)\alpha_{n1} + \boldsymbol{p}_{m0}(\boldsymbol{\xi}, \Gamma^e)\alpha_{m0} + \boldsymbol{p}_{m1}(\boldsymbol{\xi}, \Gamma^e)\alpha_{n0}}_{\boldsymbol{u}_\alpha^h}, \qquad (3)$$

where $\boldsymbol{d}_a = [u_{xa}, u_{ya}]^T$, $\boldsymbol{u}_d^h$ is standard displacement approximation, and $\boldsymbol{u}_\alpha^h$ is enriched displacement due to the introduction of strong discontinuity. The vectors $\boldsymbol{p}_{n0}(\boldsymbol{\xi}, \Gamma^e)$, $\boldsymbol{p}_{n1}(\boldsymbol{\xi}, \Gamma^e)$, $\boldsymbol{p}_{m0}(\boldsymbol{\xi}, \Gamma^e)$ and $\boldsymbol{p}_{m1}(\boldsymbol{\xi}, \Gamma^e)$ will be derived below.

2.1.2 Separation modes along the discontinuity line

With the above introduced four discontinuity parameters, we are in a position to model four independent modes of element separation along the line Γ^e (see Figure 2). These modes are named as:

1. "$n0$" - separation in direction of $\boldsymbol{n} = [n_x, n_y]^T$; separation is constant along the line,

2. "$n1$" - separation in direction of $\boldsymbol{n}$; separation is linear along the line,

3. "$m0$" - separation in direction of $\boldsymbol{m} = [m_x, m_y]^T$; separation is constant along the line,

4. "$m1$" - separation in direction of $\boldsymbol{m}$; separation is linear along the line.

One can assume a situation, when the displacements of two parts of the finite element, Ω^{e+} and Ω^{e+}, are defined only by a particular separation mode. The displacement field (3) is then given as

$$\boldsymbol{u}^h = \boldsymbol{u}^h_{mode} = \boldsymbol{u}^h_{d,mode} + \boldsymbol{u}^h_{\alpha,mode}; \quad \boldsymbol{u}^h_{\alpha,mode} = \boldsymbol{p}_{mode}\alpha_{mode}, \tag{4}$$

where $mode \in \{n0, n1, m0, m1\}$. In view of (4), the interpolation vector $\boldsymbol{p}_{mode}$ is defined as

$$\boldsymbol{p}_{mode} = \frac{\boldsymbol{u}^h_{mode} - \boldsymbol{u}^h_{d,mode}}{\alpha_{mode}}. \tag{5}$$

The vectors in (5) can be determined by examining separation modes on Figure 2, and are given as follows:

1. For mode "n_0":

$$\boldsymbol{d}_{a,n0} = \begin{cases} \boldsymbol{n}\alpha_{n0} & \text{if } a \in \Omega^{e+} \\ \boldsymbol{0} & \text{otherwise} \end{cases},$$

$$\boldsymbol{u}^h_{n0} = H_\Gamma(\boldsymbol{x})\boldsymbol{n}\alpha_{n0},$$

$$\boldsymbol{u}^h_{d,n0} = \sum_{a\in\Omega^{e+}} N_a \boldsymbol{d}_{a,n0},$$

$$\boldsymbol{p}_{n0} = \frac{\boldsymbol{u}^h_{n0} - \boldsymbol{u}^h_{d,n0}}{\alpha_{n0}} = \left(H_\Gamma(\boldsymbol{x}) - \sum_{a\in\Omega^{e+}} N_a\right)\boldsymbol{n}. \tag{6}$$

2. For mode "$n1$":

$$\boldsymbol{d}_{a,n1} = \begin{cases} \widehat{\boldsymbol{I}}\overline{\boldsymbol{x}}_a\alpha_{n1} & \text{if } a \in \Omega^{e+} \\ \boldsymbol{0} & \text{otherwise} \end{cases}; \quad \overline{\boldsymbol{x}_a} = \boldsymbol{x}_a - \boldsymbol{x}_\Gamma,$$

$$\boldsymbol{u}^h_{n1} = H_\Gamma(\boldsymbol{x})\widehat{\boldsymbol{I}}\overline{\boldsymbol{x}}\alpha_{n1}; \quad \overline{\boldsymbol{x}} = \boldsymbol{x} - \boldsymbol{x}_\Gamma,$$

$$\boldsymbol{u}^h_{d,n1} = \sum_{a\in\Omega^{e+}} N_a \boldsymbol{d}_{a,n1},$$

$$\boldsymbol{p}_{n1} = \frac{\boldsymbol{u}^h_{n1} - \boldsymbol{u}^h_{d,n1}}{\alpha_{n1}} = H_\Gamma(\boldsymbol{x})\widehat{\boldsymbol{I}}\overline{\boldsymbol{x}} - \sum_{a\in\Omega^{e+}} N_a\widehat{\boldsymbol{I}}\overline{\boldsymbol{x}}_a. \tag{7}$$

3. For mode "$m0$":

$$\boldsymbol{d}_{a,m0} = \begin{cases} \boldsymbol{m}\alpha_{m0} & \text{if } a \in \Omega^{e+} \\ \boldsymbol{0} & \text{otherwise} \end{cases},$$

$$\boldsymbol{u}^h_{m0} = H_\Gamma(\boldsymbol{x})\boldsymbol{m}\alpha_{m0},$$

$$\boldsymbol{u}^h_{d,m0} = \sum_{a\in\Omega^{e+}} N_a \boldsymbol{d}_{a,m0},$$

$$\boldsymbol{p}_{m0} = \frac{\boldsymbol{u}^h_{m0} - \boldsymbol{u}^h_{d,m0}}{\alpha_{m0}} = \left(H_\Gamma(\boldsymbol{x}) - \sum_{a\in\Omega^{e+}} N_a\right)\boldsymbol{m}. \tag{8}$$

4. For mode "$m1$":

$$d_{a,m1} = \begin{cases} (\boldsymbol{m} \cdot \overline{\boldsymbol{x}}_a) \, \boldsymbol{m} \alpha_{m1} & \text{if } a \in \Omega^{e+} \\ \boldsymbol{0} & \text{otherwise} \end{cases},$$

$$\boldsymbol{u}_{m1}^h = H_\Gamma(\boldsymbol{x}) (\boldsymbol{m} \cdot \overline{\boldsymbol{x}}) \, \boldsymbol{m} \alpha_{m1},$$

$$\boldsymbol{u}_{d,m1}^h = \sum_{a \in \Omega^{e+}} N_a \boldsymbol{d}_{a,m1},$$

$$\boldsymbol{p}_{m1} = \frac{\boldsymbol{u}_{m1}^h - \boldsymbol{u}_{d,m1}^h}{\alpha_{m1}} = \left(H_\Gamma(\boldsymbol{x}) (\boldsymbol{m} \cdot \overline{\boldsymbol{x}}) - \sum_{a \in \Omega^{e+}} N_a (\boldsymbol{m} \cdot \overline{\boldsymbol{x}}_a) \right) \boldsymbol{m}. \quad (9)$$

The following notation was used in the above equations: $H_\Gamma(\boldsymbol{x}) = \begin{cases} 1 & \text{for } \boldsymbol{x} \in \Omega^{e+} \\ 0 & \text{otherwise} \end{cases}$,

$\widehat{\boldsymbol{I}} = \begin{bmatrix} [0,-1]^T, & [1,0]^T \end{bmatrix}$. The mid-point of the discontinuity line is denoted with $\boldsymbol{x}_\Gamma$, see Figure 1. Modes "$n0$","$n1$" and "$m0$" represent rigid body motions of Ω^{e+}, while the mode "$m1$" represents a stretch of Ω^{e+}.

2.1.3 Strains

We determine the linear strain field as the symmetric gradient of (3), which can be written in a vector form as

$$\boldsymbol{\epsilon} \mid_{\Omega^e} = \left[\frac{\partial u_x^h}{\partial x}, \frac{\partial u_y^h}{\partial y}, \frac{\partial u_x^h}{\partial y} + \frac{\partial u_y^h}{\partial x} \right]^T, \quad (10)$$

or yet as

$$\boldsymbol{\epsilon} = \sum_{a=1}^4 \boldsymbol{B}_a \boldsymbol{d}_a + \boldsymbol{G}_{n0} \alpha_{n0} + \boldsymbol{G}_{n1} \alpha_{n1} + \boldsymbol{G}_{m0} \alpha_{m0} + \boldsymbol{G}_{m1} \alpha_{m1}. \quad (11)$$

Coefficients of matrices $\boldsymbol{B}_a$ and $\boldsymbol{G}_{mode}$ are derivatives of interpolation functions N_a and interpolation vectors $\boldsymbol{p}_{mode}$:

$$\boldsymbol{B}_a = \begin{bmatrix} \left[\frac{\partial N_a}{\partial x}, 0, \frac{\partial N_a}{\partial y} \right]^T, & \left[0, \frac{\partial N_a}{\partial y}, \frac{\partial N_a}{\partial x} \right]^T \end{bmatrix}, \quad (12)$$

$$\boldsymbol{G}_{n0} = \underbrace{- \sum_{a \in \Omega^{e+}} \boldsymbol{B}_a \boldsymbol{n}}_{\overline{\boldsymbol{G}}_{n0}} + \underbrace{\delta_\Gamma(\boldsymbol{x}) \boldsymbol{B}_n \boldsymbol{n}}_{\overline{\overline{\boldsymbol{G}}}_{n0}}, \quad (13)$$

$$\boldsymbol{G}_{n1} = \underbrace{- \sum_{a \in \Omega^{e+}} \boldsymbol{B}_a \widehat{\boldsymbol{I}} \overline{\boldsymbol{x}}_a}_{\overline{\boldsymbol{G}}_{n1}} + \underbrace{\delta_\Gamma(\boldsymbol{x}) \boldsymbol{B}_n \boldsymbol{n} \xi_\Gamma(\boldsymbol{x})}_{\overline{\overline{\boldsymbol{G}}}_{n1}}, \quad (14)$$

$$\boldsymbol{G}_{m0} = \underbrace{- \sum_{a \in \Omega^{e+}} \boldsymbol{B}_a \boldsymbol{m}}_{\overline{\boldsymbol{G}}_{m0}} + \underbrace{\delta_\Gamma(\boldsymbol{x}) \boldsymbol{B}_n \boldsymbol{m}}_{\overline{\overline{\boldsymbol{G}}}_{m0}}, \quad (15)$$

$$\boldsymbol{G}_{m1} = \underbrace{H_\Gamma(\boldsymbol{x}) \boldsymbol{B}_m \boldsymbol{m} - \sum_{a \in \Omega^{e+}} \boldsymbol{B}_a (\boldsymbol{m} \cdot \overline{\boldsymbol{x}}_a) \boldsymbol{m}}_{\overline{\boldsymbol{G}}_{m1}} + \underbrace{\delta_\Gamma(\boldsymbol{x}) \boldsymbol{B}_n \boldsymbol{m} \xi_\Gamma(\boldsymbol{x})}_{\overline{\overline{\boldsymbol{G}}}_{m1}}, \quad (16)$$

where

$$\delta_\Gamma \left(\boldsymbol{x} \right) = \begin{cases} \infty & \text{for } \boldsymbol{x} \in \Gamma^e \\ 0 & \text{otherwise} \end{cases} ; \quad \boldsymbol{B}_n = \left[\; [n_x, 0, n_y]^T, \quad [0, n_y, n_x]^T \; \right];$$

$$\boldsymbol{B}_m = \left[\; [m_x, 0, m_y]^T, \quad [0, m_y, m_x]^T \; \right],$$

and $\xi_\Gamma \in [-l_\Gamma/2, l_\Gamma/2]$ is a coordinate along Γ^e, which is 0 at $\boldsymbol{x}_\Gamma$ and positive in the direction of $\boldsymbol{m}$. To get the above equations, we have used the following derivation rules $\frac{\partial H_\Gamma(\boldsymbol{x})}{\partial x} = \delta_\Gamma(\boldsymbol{x})n_x$, $\frac{\partial H_\Gamma(\boldsymbol{x})}{\partial y} = \delta_\Gamma(\boldsymbol{x})n_y$ (see e.g. [9] and references therein) and expressions $\overline{\boldsymbol{x}} = \boldsymbol{x} - \boldsymbol{x}_\Gamma = \xi_\Gamma \left(\boldsymbol{x} \right) \boldsymbol{n}$, $\boldsymbol{m} \cdot \overline{\boldsymbol{x}} = \xi_\Gamma \left(\boldsymbol{x} \right)$. We further divide the strain field into a regular part $\overline{\boldsymbol{\epsilon}}$ and a singular part $\overline{\overline{\boldsymbol{\epsilon}}}$:

$$\boldsymbol{\epsilon} = \overline{\boldsymbol{\epsilon}} + \overline{\overline{\boldsymbol{\epsilon}}}, \tag{17}$$

$$\overline{\boldsymbol{\epsilon}} = \sum_{a=1}^{4} \boldsymbol{B}_a \boldsymbol{d}_a + \overline{\boldsymbol{G}}_{n0}\alpha_{n0} + \overline{\boldsymbol{G}}_{n1}\alpha_{n1} + \overline{\boldsymbol{G}}_{m0}\alpha_{m0} + \overline{\boldsymbol{G}}_{m1}\alpha_{m1}, \tag{18}$$

$$\overline{\overline{\boldsymbol{\epsilon}}} = \overline{\overline{\boldsymbol{G}}}_{n0}\alpha_{n0} + \overline{\overline{\boldsymbol{G}}}_{n1}\alpha_{n1} + \overline{\overline{\boldsymbol{G}}}_{m0}\alpha_{m0} + \overline{\overline{\boldsymbol{G}}}_{m1}\alpha_{m1}. \tag{19}$$

The singular part is just a particular representation of localized deformation at the discontinuity line.

2.1.4 Virtual strains

The interpolation of virtual strains, $\hat{\boldsymbol{\epsilon}}$, which will be used when defining weak form of equilibrium equations, is carried out according to

$$\hat{\boldsymbol{\epsilon}} \mid_{\Omega^e} = \sum_{a=1}^{4} \boldsymbol{B}_a \hat{\boldsymbol{d}}_a + \hat{\boldsymbol{G}}_{n0}\hat{\alpha}_{n0} + \hat{\boldsymbol{G}}_{n1}\hat{\alpha}_{n1} + \hat{\boldsymbol{G}}_{m0}\hat{\alpha}_{m0} + \hat{\boldsymbol{G}}_{m1}\hat{\alpha}_{m1}, \tag{20}$$

where $(\hat{\circ})$ defines a virtual parameter in contrast to the real one $(\circ)$. The kinematic enrichment of the standard quadrilateral element, which leads to real strains (18), (19) and virtual strains (20), is viewed here in the manner of the incompatible modes (e.g. Ibrahimbegovic and Wilson [15]). Therefore, the virtual strain matrices in (20) are modified according to the incompatible mode concept as

$$\hat{\boldsymbol{G}}_{\text{mode}} = \boldsymbol{G}_{\text{mode}} - \frac{1}{A_{\Omega^e}} \int_{\Omega^e} \boldsymbol{G}_{\text{mode}} d\Omega, \tag{21}$$

6

which ensures the convergence of the derived element in the spirit of the patch test. A_{Ω^e} is the area of the element. By using (21) in (13)-(16) we obtain

$$
\hat{\boldsymbol{G}}_{n0} = \underbrace{\overline{\boldsymbol{G}}_{n0} - \frac{1}{A_{\Omega^e}} \int_{\Omega^e} \overline{\boldsymbol{G}}_{n0} d\Omega - \frac{l_\Gamma}{A_{\Omega^e}} \boldsymbol{B}_n \boldsymbol{n}}_{\overline{\overline{\boldsymbol{G}}}_{n0}} + \underbrace{\delta_\Gamma\left(\boldsymbol{x}\right) \boldsymbol{B}_n \boldsymbol{n}}_{\overline{\overline{\overline{\boldsymbol{G}}}}_{n0}}, \tag{22}
$$

$$
\hat{\boldsymbol{G}}_{n1} = \underbrace{\overline{\boldsymbol{G}}_{n1} - \frac{1}{A_{\Omega^e}} \int_{\Omega^e} \overline{\boldsymbol{G}}_{n1} d\Omega}_{\overline{\overline{\boldsymbol{G}}}_{n1}} + \underbrace{\delta_\Gamma\left(\boldsymbol{x}\right) \boldsymbol{B}_n \boldsymbol{n} \xi_\Gamma\left(\boldsymbol{x}\right)}_{\overline{\overline{\overline{\boldsymbol{G}}}}_{n1}}, \tag{23}
$$

$$
\hat{\boldsymbol{G}}_{m0} = \underbrace{\overline{\boldsymbol{G}}_{m0} - \frac{1}{A_{\Omega^e}} \int_{\Omega^e} \overline{\boldsymbol{G}}_{m0} d\Omega - \frac{l_\Gamma}{A_{\Omega^e}} \boldsymbol{B}_n \boldsymbol{m}}_{\overline{\overline{\boldsymbol{G}}}_{m0}} + \underbrace{\delta_\Gamma\left(\boldsymbol{x}\right) \boldsymbol{B}_n \boldsymbol{m}}_{\overline{\overline{\overline{\boldsymbol{G}}}}_{m0}}, \tag{24}
$$

$$
\hat{\boldsymbol{G}}_{m1} = \underbrace{\overline{\boldsymbol{G}}_{m1} - \frac{1}{A_{\Omega^e}} \int_{\Omega^e} \overline{\boldsymbol{G}}_{m1} d\Omega}_{\overline{\overline{\boldsymbol{G}}}_{m1}} + \underbrace{\delta_\Gamma\left(\boldsymbol{x}\right) \boldsymbol{B}_n \boldsymbol{m} \xi_\Gamma\left(\boldsymbol{x}\right)}_{\overline{\overline{\overline{\boldsymbol{G}}}}_{m1}}. \tag{25}
$$

The modification (21) provides $\int_{\Omega^e} \hat{\boldsymbol{G}}_{\mathrm{mode}} d\Omega = 0$.

2.2 Constitutive equations

2.2.1 Material of the element bulk

We chose to model the material of the bulk of the element $\Omega^e \setminus \Gamma^e$ by classical plane stress elastoplasticity with isotropic hardening (e.g. [4]). Accordingly, the regular strains $\overline{\boldsymbol{\epsilon}}$ (18) at $\boldsymbol{x}^h \in \Omega^e \setminus \Gamma^e$ are additively decomposed into elastic part $\overline{\boldsymbol{\epsilon}}^e$ and plastic part $\overline{\boldsymbol{\epsilon}}^p$

$$
\overline{\boldsymbol{\epsilon}} = \overline{\boldsymbol{\epsilon}}^e + \overline{\boldsymbol{\epsilon}}^p, \tag{26}
$$

and the free energy is a sum of the strain energy function $\overline{W}$ and the hardening potential $\overline{\Xi}$

$$
\overline{\Psi}(\overline{\boldsymbol{\epsilon}}^e, \overline{\xi}) = \overline{W}\left(\overline{\boldsymbol{\epsilon}}^e\right) + \overline{\Xi}(\overline{\xi}) = \frac{t}{2} \overline{\boldsymbol{\epsilon}}^{eT} \boldsymbol{C} \overline{\boldsymbol{\epsilon}}^e + \overline{\Xi}(\overline{\xi}), \tag{27}
$$

where

$$
\boldsymbol{C} = \frac{E}{1-\nu^2} \left[\; [1, \nu, 0]^T, \quad [\nu, 1, 0]^T, \quad [0, 0, \tfrac{1-\nu}{2}]^T \; \right], \tag{28}
$$

E is elastic modulus, ν is Poisson's ratio, t is thickness of 2d body, and $\overline{\xi} \geq 0$ is strain-like hardening variable. We use the von Mises yield function, which can be for the plane stress written in a non-dimensional form as

$$
\overline{\phi}\left(\boldsymbol{\sigma}, \overline{q}\right) = \boldsymbol{\sigma}^T \boldsymbol{A} \boldsymbol{\sigma} - \left(1 - \frac{\overline{q}}{\sigma_y}\right)^2, \tag{29}
$$

where $\boldsymbol{\sigma} = [\sigma_{xx}, \sigma_{yy}, \sigma_{xy}]^T$ is vector of stresses,

$$
\boldsymbol{A} = \frac{1}{2\sigma_y^2} \left[\; [2, -1, 0]^T, \quad [-1, 2, 0]^T, \quad [0, 0, 6]^T \; \right], \tag{30}
$$

$\overline{q}$ is the stress like hardening variable related to $\overline{\xi}$, and σ_y is the uniaxial yield stress.

The remaining ingredients of the elastoplasticity with hardening can be obtained by consideration of thermodynamics of associative plasticity and the principle of maximum plastic dissipation (see e.g. [1], [5]). By using (26) and (27), the mechanical dissipation can be written as

$$0 \le \overline{D} \stackrel{def.}{=} \boldsymbol{\sigma}^T \dot{\overline{\boldsymbol{\epsilon}}} - \dot{\overline{\Psi}}(\overline{\boldsymbol{\epsilon}}^e, \overline{\xi}) = (\boldsymbol{\sigma} - \frac{\partial \overline{\Psi}}{\partial \overline{\boldsymbol{\epsilon}}^e})^T \dot{\overline{\boldsymbol{\epsilon}}}^e + \boldsymbol{\sigma}^T \dot{\overline{\boldsymbol{\epsilon}}}^p - \frac{\partial \overline{\Psi}}{\partial \overline{\xi}} \dot{\overline{\xi}}, \qquad (31)$$

where $(\dot{o}) = \partial(o)/\partial\tau$ and $\tau \in [0, T]$ is a pseudo-time. By assuming that the elastic process is non-dissipative (i.e. $\overline{D} = 0$), and that the plastic state variables do not change, we obtain from (31) $\boldsymbol{\sigma} = \frac{\partial \overline{\Psi}}{\partial \overline{\boldsymbol{\epsilon}}^e} = \boldsymbol{C} \overline{\boldsymbol{\epsilon}}^e$. We can define the hardening variable $\overline{q}$ by further considering (31) as $\overline{q} = -\frac{\partial \overline{\Psi}}{\partial \overline{\xi}} = -\frac{\partial \overline{\overline{\Xi}}}{\partial \overline{\xi}}$. Now, the plastic dissipation can be written as

$$\overline{D}^p = \boldsymbol{\sigma}^T \dot{\overline{\boldsymbol{\epsilon}}}^p + \overline{q} \dot{\overline{\xi}}. \qquad (32)$$

The principle of maximum plastic dissipation states that among all the variables $(\boldsymbol{\sigma}, \overline{q})$ that satisfy the yield criteria $\overline{\phi}(\boldsymbol{\sigma}, \overline{q}) \le 0$, one should choose those that maximize plastic dissipation (at frozen rates $\dot{\overline{\boldsymbol{\epsilon}}}^p$ and $\dot{\overline{\xi}}$). This can be written as a constrained optimization problem:

$$\min_{\boldsymbol{\sigma}, \overline{q}} \max_{\dot{\overline{\gamma}}} \left[\overline{L}^p(\boldsymbol{\sigma}, \overline{q}, \dot{\overline{\gamma}}) = -\overline{D}^p(\boldsymbol{\sigma}, \overline{q}) + \dot{\overline{\gamma}} \overline{\phi}(\boldsymbol{\sigma}, \overline{q}) \right], \qquad (33)$$

where $\dot{\overline{\gamma}} \ge 0$ plays the role of Lagrange multiplier. By using (32) and (29), the last result can provide the evolution equations for internal variables

$$\frac{\partial \overline{L}^p}{\partial \boldsymbol{\sigma}} = -\dot{\overline{\boldsymbol{\epsilon}}}^p + \dot{\overline{\gamma}} \frac{\partial \overline{\phi}}{\partial \boldsymbol{\sigma}} = 0 \implies \dot{\overline{\boldsymbol{\epsilon}}}^p = \dot{\overline{\gamma}} 2 \boldsymbol{A} \boldsymbol{\sigma}, \qquad (34)$$

$$\frac{\partial \overline{L}^p}{\partial \overline{q}} = -\dot{\overline{\xi}} + \dot{\overline{\gamma}} \frac{\partial \overline{\phi}}{\partial \overline{q}} = 0 \implies \dot{\overline{\xi}} = \dot{\overline{\gamma}} \frac{2}{\sigma_y} \left(1 - \frac{\overline{q}}{\sigma_y} \right) \stackrel{(29)}{=} \dot{\overline{\gamma}} \frac{2}{\sigma_y} \sqrt{\boldsymbol{\sigma}^T \boldsymbol{A} \boldsymbol{\sigma}}, \quad (35)$$

along with the Kuhn-Tucker loading/unloading conditions and the consistency condition

$$\dot{\overline{\gamma}} \ge 0, \quad \overline{\phi} \le 0, \quad \dot{\overline{\gamma}} \overline{\phi} = 0, \quad \dot{\overline{\gamma}} \dot{\overline{\phi}} = 0. \qquad (36)$$

2.2.2 Localized softening plasticity at the discontinuity line

We choose to model the material failure at the discontinuity line as plastic with softening. The failure criterion at $\boldsymbol{x}^h \in \Gamma^e$ is defined in terms of failure function

$$\overline{\overline{\phi}} = \overline{\overline{\phi}}(\boldsymbol{t}, \overline{\overline{q}}), \qquad (37)$$

where $\boldsymbol{t} = [t_n, t_m]^T$ are traction stresses, $\overline{\overline{q}}(\overline{\overline{\xi}})$ is the stress-like softening variable, and $\overline{\overline{\xi}}$ is the strain-like softening variable. Definition of traction stresses, and relationship between the traction stresses at Γ^e and the stresses in the bulk, will be provided in next section. Also, some possible forms of $\overline{\overline{\phi}}$ will be used later. As conjugant variables to the traction stresses $\boldsymbol{t}$ we choose jumps in

displacements $\overline{\overline{\boldsymbol{u}}} = [\overline{\overline{u}}_n, \overline{\overline{u}}_m]^T$ (see Figure 3), which can be expressed by jump-in-displacement parameters introduced above. The strain energy function is assumed as $\overline{\overline{\Psi}}(\overline{\overline{\xi}}) = \overline{\overline{\Xi}}(\overline{\overline{\xi}})$, where $\overline{\overline{\Xi}}$ is the softening potential. The dissipation can be then written as:

$$0 \leq \overline{\overline{D}} \overset{def.}{=} \boldsymbol{t}^T \dot{\overline{\overline{\boldsymbol{u}}}} - \dot{\overline{\overline{\Psi}}}(\overline{\overline{\xi}}) = \boldsymbol{t}^T \dot{\overline{\overline{\boldsymbol{u}}}} - \frac{\partial \overline{\overline{\Psi}}}{\partial \overline{\overline{\xi}}} \dot{\overline{\overline{\xi}}}. \tag{38}$$

By defining $\overline{\overline{q}} = -\frac{\partial \overline{\overline{\Psi}}}{\partial \overline{\overline{\xi}}} = -\frac{\partial \overline{\overline{\Xi}}}{\partial \overline{\overline{\xi}}}$, the result in (38) can be rewritten as

$$\overline{\overline{D}} = \overline{\overline{D}}^p = \boldsymbol{t}^T \dot{\overline{\overline{\boldsymbol{u}}}} + \overline{\overline{q}} \dot{\overline{\overline{\xi}}}. \tag{39}$$

The principle of maximum plastic dissipation can then be defined as:

$$\min_{\boldsymbol{t}, \overline{\overline{q}}} \max_{\dot{\overline{\overline{\gamma}}}} \left[\overline{\overline{L}}^p (\boldsymbol{t}, \overline{\overline{q}}, \dot{\overline{\overline{\gamma}}}) = -\overline{\overline{D}}^p (\boldsymbol{t}, \overline{\overline{q}}) + \dot{\overline{\overline{\gamma}}} \overline{\overline{\phi}}(\boldsymbol{t}, \overline{\overline{q}}) \right], \tag{40}$$

where $\dot{\overline{\overline{\gamma}}} \geq 0$ is the Lagrange multiplier. By using (39) and (37), we get from (40) above the following evolution equations:

$$\frac{\partial \overline{\overline{L}}^p}{\partial \boldsymbol{t}} = -\dot{\overline{\overline{\boldsymbol{u}}}} + \dot{\overline{\overline{\gamma}}} \frac{\partial \overline{\overline{\phi}}}{\partial \boldsymbol{t}} = 0 \Longrightarrow \dot{\overline{\overline{\boldsymbol{u}}}} = \dot{\overline{\overline{\gamma}}} \frac{\partial \overline{\overline{\phi}}}{\partial \boldsymbol{t}}, \tag{41}$$

$$\frac{\partial \overline{\overline{L}}^p}{\partial \overline{\overline{q}}} = -\dot{\overline{\overline{\xi}}} + \dot{\overline{\overline{\gamma}}} \frac{\partial \overline{\overline{\phi}}}{\partial \overline{\overline{q}}} = 0 \Longrightarrow \dot{\overline{\overline{\xi}}} = \dot{\overline{\overline{\gamma}}} \frac{\partial \overline{\overline{\phi}}}{\partial \overline{\overline{q}}}. \tag{42}$$

The Kuhn-Tucker loading/unloading conditions and the consistency condition also apply:

$$\dot{\overline{\overline{\gamma}}} \geq 0, \quad \overline{\overline{\phi}} \leq 0, \quad \dot{\overline{\overline{\gamma}}} \overline{\overline{\phi}} = 0, \quad \dot{\overline{\overline{\gamma}}} \dot{\overline{\overline{\phi}}} = 0. \tag{43}$$

2.3 Equilibrium equations

2.3.1 Global equations

Let a 2d body be discretized by the finite element mesh of N_{el} quadrilateral elements with embedded discontinuity in displacements. The weak form of the equilibrium equations (the principle of virtual work) can be for such a discretization written as:

$$\mathbb{A}_{e=1}^{N_{el}} \left(G^{int,e} - G^{ext,e} \right) = 0, \tag{44}$$

where $\mathbb{A}$ is the finite element assembly operator, $G^{ext,e}$ is the virtual work of external forces that are acting on a finite element, and $G^{int,e}$ is element's virtual work of internal forces, defined as

$$G^{int,e} = t^e \int_{\Omega^e} \hat{\boldsymbol{\epsilon}}^T \boldsymbol{\sigma} \, d\Omega. \tag{45}$$

Here, t^e is element's thickness (assumed as constant), and $\hat{\boldsymbol{\epsilon}}$ is vector of virtual strains. By using (20), we can write (45) as:

$$
G^{int,e} = \underbrace{\underbrace{\sum_{a=1}^{4} t^e \int_{\Omega^e} \hat{\boldsymbol{d}}_a^{\,T} \boldsymbol{B}_a^T \boldsymbol{\sigma}\ d\Omega +}_{\sum_{a=1}^{4} \hat{\boldsymbol{d}}_a^{\,T} \boldsymbol{f}_a^{int,e}}}_{\text{standard part}}
$$

$$
\underbrace{t^e \int_{\Omega^e} \left(\hat{\alpha}_{n0} \hat{\boldsymbol{G}}_{n0}^T + \hat{\alpha}_{n1} \hat{\boldsymbol{G}}_{n1}^T + \hat{\alpha}_{m0} \hat{\boldsymbol{G}}_{m0}^T + \hat{\alpha}_{m1} \hat{\boldsymbol{G}}_{m1}^T \right) \boldsymbol{\sigma}\ d\Omega}_{\text{additional part}}. \quad (46)
$$

From the term in (46), named "standard part", we obtain vector of element's internal nodal forces

$$
\boldsymbol{f}^{int,e} = \left[\boldsymbol{f}_a^{int,e,T} \right]^T; \quad \boldsymbol{f}_a^{int,e} = t^e \int_{\Omega^e} \boldsymbol{B}_a^T \boldsymbol{\sigma}\ d\Omega. \quad (47)
$$

From the virtual work of external forces $G^{ext,e}$ we get, by using standard procedure, a vector of element's external nodal forces $\boldsymbol{f}^{ext,e}$

$$
G^{ext,e} = \sum_{a=1}^{4} \hat{\boldsymbol{d}}_a^{\,T} \boldsymbol{f}_a^{ext,e}; \quad \boldsymbol{f}^{ext,e} = \left[\boldsymbol{f}_a^{ext,e,T} \right]^T, \quad (48)
$$

that represents external loading applied to that element. The discontinuity line parameters do not contribute to the external load vector. The finite element assembly of vectors $\boldsymbol{f}^{int,e}$ and $\boldsymbol{f}^{ext,e}$ leads, in view of (44), to the set of global equations that are related to the nodes of the finite element mesh

$$
\mathbb{A}_{e=1}^{N_{el}} \left(\boldsymbol{f}^{int,e} - \boldsymbol{f}^{ext,e} \right) = \boldsymbol{0}. \quad (49)
$$

2.3.2 Local equations

We have not used the term in (46) named "additional part", when constructing the set of global equations (49). We will rather treat the contribution of that term to the internal virtual work locally, on an element-by-element level. We thus have to consider the following equation

$$
t^e \int_{\Omega^e} \left(\hat{\alpha}_{n0} \hat{\boldsymbol{G}}_{n0}^T + \hat{\alpha}_{n1} \hat{\boldsymbol{G}}_{n1}^T + \hat{\alpha}_{m0} \hat{\boldsymbol{G}}_{m0}^T + \hat{\alpha}_{m1} \hat{\boldsymbol{G}}_{m1}^T \right) \boldsymbol{\sigma}\ d\Omega = 0; \qquad e = 1, 2, ... N_{el},
$$
$$
(50)
$$

for each element of the chosen mesh, which can be transformed to four equivalent expressions by using (22) to (25), and $\int_{\Omega^e} \delta_\Gamma (\circ) \, d\Omega = \int_{\Gamma^e} (\circ) \, d\Gamma$:

$$h_{n0}^e \;\; = \;\; \underbrace{t^e \int_{\Omega^e} \overline{\hat{\boldsymbol{G}}}_{n0}^T \boldsymbol{\sigma} d\Omega}_{h_{n0}^{\Omega^e}} + t^e \int_{\Gamma^e} \underbrace{\boldsymbol{n}^T \boldsymbol{B}_n^T \boldsymbol{\sigma}}_{=t_n} d\Gamma = 0, \tag{51}$$

$$\underbrace{\qquad\qquad\qquad\qquad\qquad}_{h_{n0}^{\Gamma^e}}$$

$$h_{n1}^e \;\; = \;\; \underbrace{t^e \int_{\Omega^e} \overline{\hat{\boldsymbol{G}}}_{n1}^T \boldsymbol{\sigma} d\Omega}_{h_{n1}^{\Omega^e}} + t^{(e)} \int_{\Gamma^e} \xi_\Gamma \underbrace{\boldsymbol{n}^T \boldsymbol{B}_n^T \boldsymbol{\sigma}}_{=t_n} d\Gamma = 0, \tag{52}$$

$$\underbrace{\qquad\qquad\qquad\qquad\qquad}_{h_{n1}^{\Gamma^e}}$$

$$h_{m0}^e \;\; = \;\; \underbrace{t^e \int_{\Omega^e} \overline{\hat{\boldsymbol{G}}}_{m0}^T \boldsymbol{\sigma} d\Omega}_{h_{m0}^{\Omega^e}} + t^{(e)} \int_{\Gamma^e} \underbrace{\boldsymbol{m}^T \boldsymbol{B}_n^T \boldsymbol{\sigma}}_{=t_m} d\Gamma = 0, \tag{53}$$

$$\underbrace{\qquad\qquad\qquad\qquad\qquad}_{h_{m0}^{\Gamma^e}}$$

$$h_{m1}^e \;\; = \;\; \underbrace{t^e \int_{\Omega^e} \overline{\hat{\boldsymbol{G}}}_{m1}^T \boldsymbol{\sigma} d\Omega}_{h_{m1}^{\Omega^e}} + t^{(e)} \int_{\Gamma^e} \xi_\Gamma \underbrace{\boldsymbol{m}^T \boldsymbol{B}_n^T \boldsymbol{\sigma}}_{=t_m} d\Gamma = 0. \tag{54}$$

$$\underbrace{\qquad\qquad\qquad\qquad\qquad}_{h_{m1}^{\Gamma^e}}$$

In the above equations, the traction stresses at the discontinuity line were defined as $t_n = \boldsymbol{n}^T \boldsymbol{B}_n^T \boldsymbol{\sigma} \mid_{\Gamma^e}$ and $t_m = \boldsymbol{m}^T \boldsymbol{B}_n^T \boldsymbol{\sigma} \mid_{\Gamma^e}$, with t_n and t_m representing normal and tangential components of $\boldsymbol{t}$

$$\boldsymbol{t} \mid_{\Gamma^e} = [t_n, t_m]^T. \tag{55}$$

Equations (51)-(54) provide clear relationship between the traction stresses and the stresses in the bulk. It is obvious from those equations that if one or both of the traction stresses decreases, the stresses in the bulk will decrease as well. We may gather the equations (51)-(54) in a vector form as

$$\boldsymbol{h}^{(e)} \;\; = \;\; \boldsymbol{h}^{\Omega^e} + \boldsymbol{h}^{\Gamma^e} = \left[h_{n0}^{\Omega^e}, h_{n1}^{\Omega^e}, h_{m0}^{\Omega^e}, h_{m1}^{\Omega^e} \right]^T + \left[h_{n0}^{\Gamma^e}, h_{n1}^{\Gamma^e}, h_{m0}^{\Gamma^e}, h_{m1}^{\Gamma^e} \right]^T = \boldsymbol{0} \tag{56}$$

$$e \;\; = \;\; 1, 2, ... N_{el}.$$

In order to solve (44), the set of global equilibrium equations (49), related to the nodes of the finite element mesh, has to be solved together with the set of local equilibrium equations (56), related to the elements of the mesh. The solution consists of nodal displacements of the mesh and discontinuity parameters of each finite element. Due to the chosen local treatment of displacement jumps, the displacement jumps are not continuos across the finite element edges.

2.3.3 Integration rules

The 2×2 Gauss integration scheme is used to evaluate area integrals $\int_{\Omega^e} g(x, y) \, d\Omega$, and the 2-point Gauss integration scheme is used to evaluate line integrals $\int_{\Gamma^e} f(\xi_\Gamma) \, d\Gamma$ in (51)-(54), see Figure 4. The integration along the discontinuity line is thus carried out as

$$\int_{-\frac{l_\Gamma}{2}}^{\frac{l_\Gamma}{2}} f(\xi_\Gamma) d\xi = \sum_{dip=1}^2 f(\xi_\Gamma^{dip}) w^{dip} \frac{l_\Gamma}{2}; \;\; \xi_\Gamma^{dip} = \pm \frac{l_\Gamma}{2\sqrt{3}}; \;\; w^{dip} = 1, \tag{57}$$

11

where $f(\xi_\Gamma)$ is a scalar function, $f(\xi_\Gamma^{dip})$ is its value at $\xi_\Gamma = \xi_\Gamma^{dip}$, w^{dip} is its corresponding weight, and l_Γ is length of the discontinuity line. By using (57), the $\boldsymbol{h}^{\Gamma^e}$ of (56) can be transformed to

$$\boldsymbol{h}^{\Gamma^e} = \frac{t^e l_\Gamma}{2} \left[t_{n,1} + t_{n,2}; \xi_{\Gamma,1} t_{n,1} + \xi_{\Gamma,2} t_{n,2}; t_{m,1} + t_{m,2}; \xi_{\Gamma,1} t_{m,1} + \xi_{\Gamma,2} t_{m,2} \right]^T \tag{58}$$

where

$$\boldsymbol{t}_1 = [t_{n,1}, t_{m,1}]^T; \quad \boldsymbol{t}_2 = [t_{n,2}, t_{m,2}]^T \tag{59}$$

collect traction stresses at the first integration point and at the second integration point, respectively.

3 Computational issues

In this section, we present computational details related to the solution of the set of global equilibrium equations (49) along with the set of local equilibrium equations (56). The solution is searched for at discrete pseudo-time values $0, \tau_1, \tau_2, \ldots, \tau_{n-1}, \tau_n, \tau_{n+1}, \ldots, T$ by means of the incremental-iterative scheme. We will consider a single-step scheme providing solution in a typical pseudo-time increment from τ_n to τ_{n+1}. Let us assume that the following variables of an element e, its bulk integration points $bip = 1, 2, 3, 4$, and its discontinuity integration points $dip = 1, 2$, are given at τ_n, i.e.

given: $\qquad \boldsymbol{d}_n^e = \left[\boldsymbol{d}_{a,n}^{e^T} \right]^T, \boldsymbol{\alpha}_n^e, \ \overline{\boldsymbol{\varepsilon}}_n^{p,bip}, \ \overline{\xi}_n^{bip}, \overline{\overline{\xi}}_n^{dip}$ (and sometimes $x_{\Gamma S}, \ x_{\Gamma E})$ (60)

$$e = 1, 2, \ldots N_{el} \tag{61}$$

Here, $(\circ)_n$ denotes value of $(\circ)$ at τ_n, $\boldsymbol{\alpha}_n^e = \left[\alpha_{n0,n}^e, \alpha_{n1,n}^e, \alpha_{m0,n}^e, \alpha_{m1,n}^e \right]^T$ is vector of discontinuity-line parameters, $x_{\Gamma S}$ is the starting point of the discontinuity line, $x_{\Gamma E}$ is the end point of the discontinuity line, and the other variables are described above. We will then iterate in the pseudo-time step in order to compute the converged values of the variables at τ_{n+1}, i.e.

find: $\boldsymbol{d}_{n+1}^e, \boldsymbol{\alpha}_{n+1}^e, \ \overline{\boldsymbol{\varepsilon}}_{n+1}^{p,bip}, \ \overline{\xi}_{n+1}^{bip}, \ \overline{\overline{\xi}}_{n+1}^{dip}$ (and, if necessary $x_{\Gamma S}, x_{\Gamma E}$). (62)

The computation of solution (62) is split into two phases:

a Global (mesh related) phase solves (49) for the current iterative values (with i as the iteration counter) of nodal displacements at τ_{n+1}, while keeping the other variables fixed, i.e.

global phase: $\boldsymbol{d}_{n+1}^{e,i} = \boldsymbol{d}_{n+1}^{e,i-1} + \Delta \boldsymbol{d}_{n+1}^{e,i-1}.$ (63)

The computation of iterative update $\Delta \boldsymbol{d}_{n+1}^{e,i-1}$ will be explained further below.

b Local (element and integration point related) phase uses (56) and constitutive equations to compute values of $\boldsymbol{\alpha}_{n+1}^e, \overline{\boldsymbol{\varepsilon}}_{n+1}^{p,bip}, \overline{\xi}_{n+1}^{bip}$, and $\overline{\overline{\xi}}_{n+1}^{dip}$ at τ_{n+1}, while keeping $\boldsymbol{d}_{n+1}^{e,i}$ fixed. This computation procedure depends on weather the softening in the discontinuity line has been activated in the considered element or not. In the present approach, it can be based either on:

b1 hardening plasticity at $\Omega^e \setminus \Gamma^e$ or on

b2 localized softening plasticity at Γ^e.

In this work **b1** and **b2** procedures exclude each other.

3.1 Local computations at the discontinuity line

The softening plasticity procedure is carried out only in those finite elements where:

b2.1 discontinuity line has been active at the previous time step τ_n, i.e. $x_{\Gamma S}$ and $x_{\Gamma E}$ are provided,

b2.2 discontinuity line has not been active in the previous time step but the discontinuity line in one of the neighboring elements ends at the common edge, i.e. $x_{\Gamma S}$ is provided.

3.1.1 Orientation of the discontinuity line

In the **b2.2** case, we first compute orientation of the discontinuity line. Average element stresses $\boldsymbol{\sigma}^{avg}$ are used to define unit vectors $\boldsymbol{n}$ and $\boldsymbol{m}$

$$\boldsymbol{n} = \boldsymbol{n}\left(\boldsymbol{\sigma}^{avg}(\boldsymbol{d}_{n+1}^e, \overline{\boldsymbol{\varepsilon}}_n^{p,bip})\right); \quad \boldsymbol{m} = \boldsymbol{m}\left(\boldsymbol{\sigma}^{avg}(\boldsymbol{d}_{n+1}^e, \overline{\boldsymbol{\varepsilon}}_n^{p,bip})\right). \quad (64)$$

When analyzing cracking in brittle materials, the governing mode of separation is assumed as mode I. Then the normal vector $\boldsymbol{n}$ is chosen to be parallel to the direction of the maximum principal stress, and remains fixed. When analyzing metals or soils, the governing mode of separation is assumed as mode II. Then the tangential vector $\boldsymbol{m}$ is chosen to be parallel to one of two perpendicular directions of maximum shear stress. It remains fixed as well. Once the discontinuity direction is determined, we are able to obtain the end point of the discontinuity $x_{\Gamma E}$, which completes geometric description (Ω^{e-}, Ω^{e+} and l_Γ) of a finite element with active embedded discontinuity line.

3.1.2 Softening plasticity and jump-in-displacements parameters

The main part of the softening plasticity procedure is equal for both **b2.1** and **b2.2** cases. The local equilibrium equations (56) are solved together with the traction-separation constitutive relations to compute jump-in-displacement parameters and internal plasticity variables.

The procedure starts with computation of trial values of traction stresses in two integration points at the discontinuity line. Local equilibrium equations (56) are used for this purpose. We compute

$$\begin{aligned}
\boldsymbol{h}_{n+1}^{\Omega^e,trial} &= \left[\begin{array}{cccc} h_{n0,n+1}^{\Omega^e,trial}, & h_{n1,n+1}^{\Omega^e,trial}, & h_{m0,n+1}^{\Omega^e,trial}, & h_{m1,n+1}^{\Omega^e,trial} \end{array}\right]^T = \quad (65)\\
&\quad \boldsymbol{h}^{\Omega^e}\left(\boldsymbol{\sigma}(\boldsymbol{d}_{n+1}^{e,i}, \overline{\boldsymbol{\varepsilon}}_n^{p,bip}, \boldsymbol{\alpha}_n)\right).
\end{aligned}$$

to get four algebraic equations for traction stresses at both integration points, which can be expressed as

$$\boldsymbol{h}_{n+1}^{\Omega^e,trial} + \boldsymbol{h}^{\Gamma^e}(\boldsymbol{t}_{n+1}^{1,trial}, \boldsymbol{t}_{n+1}^{2,trial}) = \boldsymbol{0}, \quad (66)$$

13

or yet as

$$\boldsymbol{t}_{n+1}^{1,trial} = \begin{bmatrix} t_{n,n+1}^{1,trial} \\ t_{m,n+1}^{1,trial} \end{bmatrix} = \frac{2}{(\xi_\Gamma^2 - \xi_\Gamma^1)l_\Gamma} \begin{bmatrix} h_{n1,n+1}^{\Omega^e,trial} - h_{n0,n+1}^{\Omega^e,trial}\xi_\Gamma^2 \\ h_{m1,n+1}^{\Omega^e,trial} - h_{m0,n+1}^{\Omega^e,trial}\xi_\Gamma^2 \end{bmatrix} ; \quad (67)$$

$$\boldsymbol{t}_{n+1}^{2,trial} = \begin{bmatrix} t_{n,n+1}^{2,trial} \\ t_{m,n+1}^{2,trial} \end{bmatrix} = \frac{2}{(\xi_\Gamma^1 - \xi_\Gamma^2)l_\Gamma} \begin{bmatrix} h_{n1,n+1}^{\Omega^e,trial} - h_{n0,n+1}^{\Omega^e,trial}\xi_\Gamma^1 \\ h_{m1,n+1}^{\Omega^e,trial} - h_{m0,n+1}^{\Omega^e,trial}\xi_\Gamma^1 \end{bmatrix} . \quad (68)$$

where ξ_Γ^1 and ξ_Γ^2 are values of ξ_Γ coordinate at both integration points. We are now in position to check trial values of failure function (37) at the discontinuity line integration points

$$\underbrace{\bar{\bar{\phi}}^{1,trial} = \bar{\bar{\phi}}(\boldsymbol{t}_{n+1}^{1,trial}, \bar{\bar{q}}(\bar{\bar{\xi}}_n^1)) \le 0 \text{ or } \bar{\bar{\phi}}^{2,trial} = \bar{\bar{\phi}}(\boldsymbol{t}_{n+1}^{2,trial}, \bar{\bar{q}}(\bar{\bar{\xi}}_n^2)) \le 0}_{?}. \quad (69)$$

If the criterion (69) is satisfied, i.e. if function $\bar{\bar{\phi}}$ is less or equal to zero in at least one integration point, the values of local variables remain unchanged

$$\bar{\bar{\phi}}^{1,trial} \le 0 \text{ or } \bar{\bar{\phi}}^{2,trial} \le 0 \implies \bar{\bar{\xi}}_{n+1}^1 = \bar{\bar{\xi}}_n^1; \ \bar{\bar{\xi}}_{n+1}^2 = \bar{\bar{\xi}}_n^2; \ \boldsymbol{\alpha}_{n+1}^e = \boldsymbol{\alpha}_n^e. \quad (70)$$

If the criterion (69) is violated, the backward Euler integration of (41) and (42) is performed

$$\bar{\bar{\boldsymbol{u}}}_{n+1}^1 = \bar{\bar{\boldsymbol{u}}}_n^1 + \bar{\bar{\gamma}}_{n+1}^1 \frac{\partial \bar{\bar{\phi}}}{\partial \boldsymbol{t}}|_{\xi_\Gamma^1}; \quad \bar{\bar{\xi}}_{n+1}^1 = \bar{\bar{\xi}}_n^1 + \bar{\bar{\gamma}}_{n+1}^1 \frac{\partial \bar{\bar{\phi}}}{\partial q}|_{\xi_\Gamma^1}; \quad (71)$$

$$\bar{\bar{\boldsymbol{u}}}_{n+1}^2 = \bar{\bar{\boldsymbol{u}}}_n^2 + \bar{\bar{\gamma}}_{n+1}^2 \frac{\partial \bar{\bar{\phi}}}{\partial \boldsymbol{t}}|_{\xi_\Gamma^2}; \quad \bar{\bar{\xi}}_{n+1}^2 = \bar{\bar{\xi}}_n^2 + \bar{\bar{\gamma}}_{n+1}^2 \frac{\partial \bar{\bar{\phi}}}{\partial q}|_{\xi_\Gamma^2}, \quad (72)$$

where $\bar{\bar{\gamma}}_{n+1}^1 = \dot{\bar{\bar{\gamma}}}_{n+1}^1(\tau_{n+1} - \tau_n)$ and $\bar{\bar{\gamma}}_{n+1}^2 = \dot{\bar{\bar{\gamma}}}_{n+1}^2(\tau_{n+1} - \tau_n)$. The values of plastic multipliers $\bar{\bar{\gamma}}_{n+1}^1$ and $\bar{\bar{\gamma}}_{n+1}^2$, which are not known in (71)-(72), are computed with an iterative solution of the system of two nonlinear equations

$$\bar{\bar{\phi}}^1 \left(\boldsymbol{t}_{n+1}^1 \left(\bar{\bar{\gamma}}_{n+1}^1, \bar{\bar{\gamma}}_{n+1}^2 \right), \bar{\bar{q}} \left(\bar{\bar{\xi}}_{n+1}^1 \left(\bar{\bar{\gamma}}_{n+1}^1 \right) \right) \right) = \bar{\bar{\phi}}^1 \left(\bar{\bar{\gamma}}_{n+1}^1, \bar{\bar{\gamma}}_{n+1}^2 \right) = 0; \quad (73)$$

$$\bar{\bar{\phi}}^2 \left(\boldsymbol{t}_{n+1}^2 \left(\bar{\bar{\gamma}}_{n+1}^1, \bar{\bar{\gamma}}_{n+1}^2 \right), \bar{\bar{q}} \left(\bar{\bar{\xi}}_{n+1}^2 \left(\bar{\bar{\gamma}}_{n+1}^2 \right) \right) \right) = \bar{\bar{\phi}}^2 \left(\bar{\bar{\gamma}}_{n+1}^1, \bar{\bar{\gamma}}_{n+1}^2 \right) = 0, \quad (74)$$

where the tractions are expressed through four algebraic equations (in the same manner as in the case of trial values)

$$\boldsymbol{h}^{\Omega^e} \left(\boldsymbol{\sigma}(\boldsymbol{d}_{n+1}^e, \bar{\boldsymbol{\varepsilon}}_n^{p,bip}, \boldsymbol{\alpha}_{n+1}^e) \right) + \boldsymbol{h}^{\Gamma^e} (\boldsymbol{t}_{n+1}^1, \boldsymbol{t}_{n+1}^2) = \boldsymbol{0} \implies \quad (75)$$
$$\boldsymbol{t}_{n+1}^1 \left(\bar{\bar{\gamma}}_{n+1}^1, \bar{\bar{\gamma}}_{n+1}^2 \right), \ \boldsymbol{t}_{n+1}^2 \left(\bar{\bar{\gamma}}_{n+1}^1, \bar{\bar{\gamma}}_{n+1}^2 \right).$$

In (75), the following relations between the jumps in displacements and the kinematic discontinuity parameters are needed

$$\boldsymbol{\alpha}_{n+1}^e(\bar{\bar{\boldsymbol{u}}}_{n+1}^1, \bar{\bar{\boldsymbol{u}}}_{n+1}^2) = \quad (76)$$
$$\left[\frac{\bar{\bar{u}}_{n,n+1}^1 + \bar{\bar{u}}_{n,n+1}^2}{2}, \frac{\bar{\bar{u}}_{n,n+1}^1 - \bar{\bar{u}}_{n,n+1}^2}{\xi_\Gamma^1 - \xi_\Gamma^2}, \frac{\bar{\bar{u}}_{m,n+1}^1 + \bar{\bar{u}}_{m,n+1}^2}{2}, \frac{\bar{\bar{u}}_{m,n+1}^1 - \bar{\bar{u}}_{m,n+1}^2}{\xi_\Gamma^1 - \xi_\Gamma^2} \right]^T,$$

14

where $\overline{\overline{\boldsymbol{u}}}_{n+1}^{1} = \left[\overline{\overline{u}}_{n,n+1}^{1}, \overline{\overline{u}}_{m,n+1}^{1}\right]^{T}$ and $\overline{\overline{\boldsymbol{u}}}^{2} = \left[\overline{\overline{u}}_{n,n+1}^{2}, \overline{\overline{u}}_{m,n+1}^{2}\right]^{T}$. When converged values of $\overline{\overline{\gamma}}_{n+1}^{1}$ and $\overline{\overline{\gamma}}_{n+1}^{2}$ are obtained from (73)-(74), updated values $\overline{\overline{u}}_{n+1}^{1}$, $\overline{\overline{u}}_{n+1}^{2}$, $\boldsymbol{\alpha}_{n+1}^{e}$, $\overline{\overline{\xi}}_{n+1}^{1}$ and $\overline{\overline{\xi}}_{n+1}^{2}$ are computed by (71), (72) and (76).

The main result of the above described softening plasticity procedure are new values of parameters $\boldsymbol{\alpha}_{n+1}^{e}$, which influence the stresses of the element bulk, since

$$\boldsymbol{\sigma}_{n+1}^{bip} = \boldsymbol{C}\left(\overline{\varepsilon}(\boldsymbol{d}_{n+1}^{e,i}, \boldsymbol{\alpha}_{n+1}^{e}) - \overline{\varepsilon}_{n+1}^{p,bip}\right), \tag{77}$$

where $\overline{\varepsilon}_{n+1}^{p,bip} = \overline{\varepsilon}_{n}^{p,bip}$.

3.2 Hardening plasticity at the element bulk

The hardening plasticity procedure **b1** is carried out at in a standard way (e.g. see [1], [3], [6] for details) at each integration point ip in order to compute internal variables. We first provide the trial values of the stresses

$$\boldsymbol{\sigma}_{n+1}^{trial,bip} = \boldsymbol{C}(\overline{\varepsilon}(\boldsymbol{d}_{n+1}^{e,i}, \boldsymbol{\alpha}_{n}^{e}) - \overline{\varepsilon}_{n}^{p,bip}), \tag{78}$$

and the trial value of the yield function $\overline{\phi}^{trial,bip}$. If the trial yield criterion

$$\overline{\phi}^{trial,bip}(\boldsymbol{\sigma}_{n+1}^{trial,bip}, \overline{q}(\overline{\xi}_{n}^{bip})) \overset{?}{\leq} 0 \tag{79}$$

is satisfied, the values of hardening plasticity local variables remain unchanged (the step is elastic)

$$\overline{\phi}^{trial,bip} \leq 0 \implies \overline{\varepsilon}_{n+1}^{p,bip} = \overline{\varepsilon}_{n}^{p,bip}; \quad \overline{\xi}_{n+1}^{bip} = \overline{\xi}_{n}^{bip}. \tag{80}$$

In the case of violation of (79), we first provide the updated values of stresses

$$\boldsymbol{\sigma}_{n+1}^{bip} = \left[\boldsymbol{I}_{3} + \overline{\gamma}_{n+1}^{bip} 2\boldsymbol{C}\boldsymbol{A}\right]^{-1} \boldsymbol{\sigma}_{n+1}^{trial,bip}. \tag{81}$$

By using the backward Euler integration scheme we update values of internal variables as

$$\overline{\varepsilon}_{n+1}^{p,bip} = \overline{\varepsilon}_{n}^{p,bip} + \overline{\gamma}_{n+1}^{bip} 2\boldsymbol{A}\boldsymbol{\sigma}_{n+1}^{bip}; \quad \overline{\xi}_{n+1}^{bip} = \overline{\xi}_{n}^{bip} + \overline{\gamma}_{n+1}^{bip} \frac{2}{\sigma_{y}} \sqrt{\left(\boldsymbol{\sigma}_{n+1}^{bip}\right)^{T} \boldsymbol{A}\boldsymbol{\sigma}_{n+1}^{bip}}, \tag{82}$$

where $\overline{\gamma}_{n+1}^{bip} = \dot{\overline{\gamma}}_{n+1}^{bip}(\tau_{n+1} - \tau_{n})$. The value of the plastic multiplier $\overline{\gamma}_{n+1}^{bip}$, which is unknown in (82), is obtained by solving nonlinear equation

$$\overline{\phi}^{ip}(\boldsymbol{\sigma}_{n+1}^{bip}(\boldsymbol{d}_{n+1}^{e,i}, \overline{\varepsilon}_{n+1}^{p,bip}(\overline{\gamma}_{n+1}^{bip})), \overline{q}(\overline{\xi}_{n+1}^{bip}(\overline{\gamma}_{n+1}^{bip}))) = \overline{\phi}^{bip}(\overline{\gamma}_{n+1}^{bip}) = 0. \tag{83}$$

The main result of the above described procedure are the admissible values of the stresses $\boldsymbol{\sigma}_{n+1}^{bip}$

$$\boldsymbol{\sigma}_{n+1}^{bip} = \boldsymbol{C}\left(\overline{\varepsilon}_{n+1}^{bip,i}(\boldsymbol{d}_{n+1}^{e,i}, \boldsymbol{\alpha}_{n+1}^{e}) - \overline{\varepsilon}_{n+1}^{p,bip}\right), \tag{84}$$

where the updated values of the discontinuity parameters are $\boldsymbol{\alpha}_{n+1}^e = \boldsymbol{\alpha}_n^e$. The elastoplastic tangent operator $\boldsymbol{C}_{n+1}^{ep,bip,i} = d\boldsymbol{\sigma}/d\overline{\boldsymbol{\varepsilon}} \mid_{n+1}^{bip,i}$ is needed in global computations. To compute $\boldsymbol{C}^{ep}$ from (84), the chain rule is applied

$$\frac{d\overline{\boldsymbol{\varepsilon}}^p}{d\overline{\boldsymbol{\varepsilon}}} \mid_{n+1}^{bip,i} = \frac{d\overline{\boldsymbol{\varepsilon}}^p}{d\overline{\gamma}} \mid_{n+1}^{bip} \frac{d\overline{\gamma}}{d\overline{\boldsymbol{\varepsilon}}} \mid_{n+1}^{bip,i}, \tag{85}$$

where derivative $d\overline{\gamma}/d\overline{\boldsymbol{\varepsilon}}$ is computed from the consistency condition $\dot{\overline{\gamma}}\dot{\overline{\phi}} \mid_{n+1}^{bip} = 0$. Since $\overline{\phi}^{ip} = \overline{\phi}^{ip}\left(\overline{\boldsymbol{\varepsilon}}_{n+1}^{bip,i}, \overline{\gamma}_{n+1}^{bip}\right)$ and $\dot{\overline{\gamma}}_{n+1}^{bip} > 0$, one has

$$\begin{aligned} \dot{\overline{\phi}}_{n+1}^{bip} &= \left(\frac{d\overline{\phi}}{d\overline{\boldsymbol{\varepsilon}}}\dot{\overline{\boldsymbol{\varepsilon}}}\right) \mid_{n+1}^{bip,i} + \left(\frac{d\overline{\phi}}{d\overline{\gamma}}\frac{d\overline{\gamma}}{d\overline{\boldsymbol{\varepsilon}}}\dot{\overline{\boldsymbol{\varepsilon}}}\right) \mid_{n+1}^{bip,i} \\ &= \underbrace{\left(\frac{d\overline{\phi}}{d\overline{\boldsymbol{\varepsilon}}} + \frac{d\overline{\phi}}{d\overline{\gamma}}\frac{d\overline{\gamma}}{d\overline{\boldsymbol{\varepsilon}}}\right) \mid_{n+1}^{bip,i}}_{0} \underbrace{\dot{\overline{\boldsymbol{\varepsilon}}} \mid_{n+1}^{bip,i}}_{\neq 0} = 0. \end{aligned} \tag{86}$$

It follows from (86)

$$\frac{d\overline{\gamma}}{d\overline{\boldsymbol{\varepsilon}}} \mid_{n+1}^{bip,i} = \left(-\left(\frac{d\overline{\phi}}{d\overline{\gamma}}\right)^{-1}\frac{d\overline{\phi}}{d\overline{\boldsymbol{\varepsilon}}}\right) \mid_{n+1}^{bip,i}, \tag{87}$$

which leads to

$$\boldsymbol{C}_{n+1}^{ep,bip,i} = \frac{d\boldsymbol{\sigma}}{d\overline{\boldsymbol{\varepsilon}}} \mid_{n+1}^{bip,i} = \boldsymbol{C}\left(\boldsymbol{I} + \frac{d\overline{\boldsymbol{\varepsilon}}^p}{d\overline{\gamma}}\left(\frac{d\overline{\phi}}{d\overline{\gamma}}\right)^{-1}\frac{d\overline{\phi}}{d\overline{\boldsymbol{\varepsilon}}}\right) \mid_{n+1}^{bip,i} \tag{88}$$

The derivatives in (88) can be computed with some manipulations from the above equations.

3.3 Global computations

Once the local variables are computed by **b** procedure, we turn to the global phase **a** of the iterative loop in order to provide, if needed, new iterative values of nodal displacements. First, the set of global equilibrium equations (49) is checked with newly computed $\boldsymbol{\sigma}_{n+1}^{bip}$ from the local phase

$$\left\|\mathbb{A}_{e=1}^{N_{el}}[\boldsymbol{f}_{n+1}^{int,e} - \boldsymbol{f}_{n+1}^{ext,e,i}]\right\| \stackrel{?}{<} tol. \tag{89}$$

If the convergence criterion (89) is satisfied, we move on to the next pseudo-time incremental step. If the convergence criterion fails, we perform a new iterative sweep within the present pseudo-time incremental step. New iterative values of nodal displacements of the finite element mesh are computed by accounting for each element contribution. A single element contribution can be written as

$$\begin{bmatrix} \boldsymbol{K}^e & \boldsymbol{K}^{f\alpha} \\ \boldsymbol{K}^{hd} & \boldsymbol{K}^{h\alpha} \end{bmatrix}_{n+1}^i \begin{pmatrix} \Delta\boldsymbol{d}_{n+1}^{e,i} \\ \Delta\boldsymbol{\alpha}_{n+1}^{e,i} \end{pmatrix} = \begin{pmatrix} \boldsymbol{f}_{n+1}^{ext,e} - \boldsymbol{f}_{n+1}^{int,e,i} \\ \boldsymbol{0} \end{pmatrix}, \tag{90}$$

where the parts of the element stiffness matrix can be formally written as

$$\begin{aligned} \boldsymbol{K}_{n+1}^{e,i} &= \left(\frac{\partial\boldsymbol{f}^{int,e}}{\partial\boldsymbol{d}^e}\right)_{n+1}^i; \quad \boldsymbol{K}_{n+1}^{f\alpha,i} = \left(\frac{\partial\boldsymbol{f}^{int,e}}{\partial\boldsymbol{\alpha}^e}\right)_{n+1}^i; \\ \boldsymbol{K}_{n+1}^{hd,i} &= \left(\frac{\partial\boldsymbol{h}^e}{\partial\boldsymbol{d}^e}\right)_{n+1}^i; \qquad \boldsymbol{K}_{n+1}^{h\alpha,i} = \left(\frac{\partial\boldsymbol{h}^e}{\partial\boldsymbol{\alpha}^e}\right)_{n+1}^i. \end{aligned} \tag{91}$$

where

$$\frac{\partial \boldsymbol{f}^{int,e}}{\partial \boldsymbol{d}^e} = \frac{\partial \boldsymbol{f}^{int,e}}{\partial \boldsymbol{\sigma}} \frac{d\boldsymbol{\sigma}}{d\overline{\boldsymbol{\varepsilon}}} \frac{\partial \overline{\boldsymbol{\varepsilon}}}{\partial \boldsymbol{d}^e}; \qquad \frac{\partial \boldsymbol{f}^{int,e}}{\partial \boldsymbol{\alpha}^e} = \frac{\partial \boldsymbol{f}^{int,e}}{\partial \boldsymbol{\sigma}} \frac{d\boldsymbol{\sigma}}{d\overline{\boldsymbol{\varepsilon}}} \frac{\partial \overline{\boldsymbol{\varepsilon}}}{\partial \boldsymbol{\alpha}^e};$$
$$\frac{\partial \boldsymbol{h}^e}{\partial \boldsymbol{d}^e} = \frac{\partial \boldsymbol{h}^e}{\partial \boldsymbol{\sigma}} \frac{d\boldsymbol{\sigma}}{d\overline{\boldsymbol{\varepsilon}}} \frac{\partial \overline{\boldsymbol{\varepsilon}}}{\partial \boldsymbol{d}^e}; \qquad \frac{\partial \boldsymbol{h}^e}{\partial \boldsymbol{\alpha}^e} = \frac{\partial \boldsymbol{h}^e}{\partial \boldsymbol{t}} \frac{d\boldsymbol{t}}{d\boldsymbol{\alpha}^e} + \frac{\partial \boldsymbol{h}^e}{\partial \boldsymbol{\sigma}} \frac{d\boldsymbol{\sigma}}{d\overline{\boldsymbol{\varepsilon}}} \frac{\partial \overline{\boldsymbol{\varepsilon}}}{\partial \boldsymbol{\alpha}^e}. \tag{92}$$

The static condensation in (90) above allows us to form the standard form of the element stiffness matrix $\widehat{\boldsymbol{K}}_{n+1}^{e,i}$ that contributes to the finite element assembly

$$\mathbb{A}_{e=1}^{N_{el}} \left(\widehat{\boldsymbol{K}}_{n+1}^{e,i} \Delta \boldsymbol{d}_{n+1}^{e,i} \right) = \mathbb{A}_{e=1}^{N_{el}} \left(\boldsymbol{f}_{n+1}^{ext,e} - \boldsymbol{f}_{n+1}^{int,e,i} \right), \tag{93}$$

where

$$\widehat{\boldsymbol{K}}_{n+1}^{e,i} = \boldsymbol{K}_{n+1}^{e,i} - \boldsymbol{K}_{n+1}^{f\alpha,i} \left(\boldsymbol{K}_{n+1}^{h\alpha,i} \right)^{-1} \boldsymbol{K}_{n+1}^{hd,i}. \tag{94}$$

Solution of (93) gives the values of iterative update $\Delta \boldsymbol{d}_{n+1}^{e,i}$, which should be used as indicated in (63).

4 Examples

The finite element code has been derived by the symbolic manipulation program AceGen [7], and incorporated into FE code AceFem [7].

4.1 Tension test

In this example we consider a square block of 20 cm × 20 cm × 0.1 cm subjected to uniaxial tension, see Figure 6. The block is made of elastic material with Young's modulus $E = 3000$ kN/cm^2, Poisson's ratio $\nu = 0.2$ and the ultimate tensile strength $\sigma_u = 0.3$ kN/cm^2. The softening response is governed by the cohesive law at the discontinuity presented in Figure 5. We can write the law in terms of failure criterion

$$\overline{\overline{\phi}}(\boldsymbol{t}, \overline{\overline{q}}) = t_n - \left(\sigma_u - \overline{\overline{q}} \right) \leq 0, \tag{95}$$

and the linear softening

$$\overline{\overline{q}} = \min \left[\sigma_u, -K_s \overline{\overline{\xi}} \right], \tag{96}$$

where $K_s = -45$ kN/cm^3 is the softening modulus. We model the block with one finite element, which is supported at the left side and pulled, by imposing displacements, at the right side (see Figure 6). Once the tensile strength of the material is reached, the discontinuity appears in the direction perpendicular to the maximum principal stress. The behavior of the discontinuity is only defined for mode I, i.e. the equations for the traction in the tangential direction and the corresponding jumps are not considered in the simulation. In Figure 7 we present the reaction force versus imposed displacement diagram. The results of the present formulation are in complete agreement with those obtained in [8], apart the local unloading branch that our rigid-plastic formulation can capture.

4.2 Bending test

We consider bending test of the block with the same material and geometrical properties as in previous example. In Figure 8 we present the problem definition. In the first part of loading process the displacement at the top u_{xT} and the

displacement at the bottom u_{xB} are applied with the same rate. The tensile strength of the material is reached at $u_{xT} = u_{xB} = 0.001$ cm and at that point the discontinuity in mode I appears. This is followed by a non-uniform regime of loading with the rate of imposed displacement at the bottom being twice the rate of imposed displacement at the top, see right side of Figure 8. In Figure 9 we present the results of our simulation along with the results obtained in [8]. The differences in results are hardly noticeable up until the point when the first fibers of the discontinuity fail completely, resulting with $t_n = 0$. After that the results no longer coincide, since the integration scheme in [8] considers five integration points along the discontinuity line and can therefore represent a smoother transition from the softening regime to the complete failure.

4.3 Partial tension test

In the above numerical examples we have evaluated the performance of the present formulation for the normal opening response. To evaluate the performance of the present formulation for the tangential response, i.e. the mode II response with linear softening at the discontinuity in its tangential direction, we consider the partial tension test presented in Figure 10. The block is of the same dimensions as in the previous examples, with the same value of Young's modulus $E = 3000$ kN/cm^2 but with Poisson's ratio $\nu = 0$. We consider a pre-existing discontinuity at the center of the block. From the beginning there is no resistance in the discontinuity line, i.e. the discontinuity line provides no stiffness in the tangential direction and the tangential traction is always zero ($t_m = 0$). The equations involving the normal response are simply left out in this simulation. Again, we model the block by using only one finite element. The block is supported at the two nodes on the left side and pulled apart at two nodes on the right side, thus causing a linear displacement distribution along the height of the Ω^+region. In this way the only stress that develops is σ_{yy}, which is only limited to Ω^+region and all the other stresses remain zero throughout the test ($\sigma_{xx} = \sigma_{xy} = \sigma_{yy}^{\Omega^-} = 0$). In Figure 11 we present the stresses that develop in the element with the increase of imposed displacements. Again we compare the results of the present work with the results obtained in [8]. The results presented in Figure 11 are in complete agreement. The stress σ_{yy} in the Ω^- region is unaffected by the imposed displacements and is always equal to zero, while the stress component σ_{yy} in the Ω^+ changes with the increase of imposed displacement according to $\sigma_{yy}^+ = \frac{E u_y}{b}$.

4.4 Three point bending test

We consider a classical benchmark problem of a notched concrete beam under three point bending. In Figure 12 we present the geometry of the specimen, a 200 cm $\times$ 20 cm $\times$ 5 cm simply supported concrete beam with a 2 cm $\times$ 10 cm $\times$ 5 cm notch placed at the bottom of the beam. The beam is loaded by downward displacement imposed at the top in its center. The beam is made of material with Young's modulus $E = 3000$ kN/cm^2, Poisson's ratio $\nu = 0.2$ and the ultimate tensile strength $\sigma_u = 0.333$ kN/cm^2. The softening response is governed by the plastic cohesive law at the discontinuity line, presented in Figure 13. The law in Figure 13 can be also written in terms of failure criterion

18

(95) and the exponential softening law

$$\bar{\bar{q}} = \sigma_u \left(1 - \exp^{-\frac{\bar{\bar{\xi}}\sigma_u}{G_f}} \right),\tag{97}$$

where $G_f = 0.124 \cdot 10^{-2}$ kN/cm is the fracture energy. The response of the discontinuity in the tangential direction is not considered in the simulations. In Figure 14 we present two different finite element meshes that were used in simulations. The coarser mesh consists of 530 finite elements and the finer one of 2186 finite elements. On the left side of Figure 15 we plot the reaction versus imposed displacement diagrams computed for both meshes. The discontinuity starts at the notch, when the tensile strength of the material is reached and propagates in the direction perpendicular to the maximum principal stress, i.e. in the mode I fashion. We have encountered a problem when using the above criterion to determine the discontinuity direction, namely the direction of the maximum principal stress at some point suddenly changes for 90 degrees. This causes a problem in convergence in the simulation with the fine mesh and a non-physical response when using the coarse mesh, see left side of Figure 15. The discontinuity direction problem was also reported in [9] and we direct the reader therein for further discussion. To obtain the solution without the discontinuity direction problem we considered a predetermined direction of the discontinuity, i.e. discontinuity can only propagate perpendicular to the length of the beam. With this modification we were able to obtain with both meshes the results that are within the experimentally established bounds, taken from [8]. The results of all simulations are given in Figure 15 (left). In the center and right side of Figure 15 we present the deformed configuration (scaled 100 times) of the area near the notch for both course and fine mesh.

4.5   Four point bending test

In this example we study the four point bending test on a beam with a notch. In Figure 16 we present the specimen geometry along with loading conditions and supports. The specimen is made of material with Young's modulus $E = 2880$ kN/cm^2, Poisson's ratio $\nu = 0.18$ and the ultimate tensile strength $\sigma_u = 0.28$ kN/cm^2. The behavior of the discontinuity is governed by the failure criterion (95) and the softening law (96), with softening modulus being $K_s = -39.2$ kN/cm^3. In Figure 17 we present the mesh that we used in simulations. With respect to the description of the displacements jumps along the discontinuity line we considered three cases: (i) "n0 + m0" - the constant jump in displacements in both normal and tangential direction, (ii) "n0 + n1" - linear jump in displacement in normal direction only and (iii) "n0" - constant jump in displacements in normal direction only. In the mixed mode case ("n0 + m0") we considered a reduced shear stiffness for the tangential response according to relation

$$\bar{\bar{\phi}}(t_m) = t_m - k_m \bar{\bar{u}}_m = 0,\tag{98}$$

where $k_m = 2.88$ kN/cm^3. The results of the simulations are presented in Figures 18 and 19. On the left side of Figure 18 we plot the applied load - crack mouth sliding displacements curves of our simulations along with the envelope of results the we adopted from [8]. We can see that all the proposed formulations give a good prediction of the limit load of the structure, while only the mixed

mode formulation can capture the true softening response of the structure. On the right side of Figure 18 we plot the crack paths that correspond to curves on the left side of the same figure. In Figure 19 we present the deformed (scaled 200 times) mesh of the area near the notch for all formulations.

4.6 Delamination of a plate

We consider a delamination test shown in Figure 20 as presented in [11]. The properties of the material are: Young's modulus $E = 50$ kN/cm^2 and Poisson ratio $\nu = 0.3$. We model the interface as an embedded discontinuity whose properties are determined with the failure criterion (95), the ultimate tension stress $\sigma_u = 10^{-1}$ kN/cm^2 and the exponential softening law (97) with the fracture energy $G_f = 5 \times 10^{-3}$ kN/cm. The simulations are performed by using a coarse and a fine finite element mesh, as presented in Figure 21. The reaction force versus imposed displacement diagrams are presented in Figure 22. One can see, that the results of both coarse and fine mesh are in good agreement with the results obtained in [11] by using a fine mesh. Figure 23 depicts the deformed meshes that correspond to the imposed displacement $u_y = 0.2$ cm. Note that the deformed meshes are not scaled and one should for a more realistic representation use a geometrically non-linear framework.

4.7 Elasto-plastic tension test

In the last example we consider a tension test of a metal strip. The geometry of the strip is presented in Figure 24. Its thickness is 0.055 cm. One of the shorter edges is built-in and the opposite edge is pulled by imposing the displacements as depicted in Figure 24. In this example we consider the bulk material as elasto-plastic with the following properties: Young's modulus $E = 21000$ kN/cm^2, Poisson's ratio $\nu = 0.3$, yield stress $\sigma_y = 40$ kN/cm^2 and hardening modulus $K_h = 1000$ kN/cm^2. We compute the stress-like variable related to isotropic hardening as

$$\bar{q} = -K_h \bar{\xi}. \tag{99}$$

The softening response is activated once the ultimate shear stress $\tau_u = 21$ kN/cm^2 is reached and then the mode II propagation of the discontinuity starts. The response of the discontinuity is governed by the cohesive law depicted in Figure 25, which can be also represented in the form of failure criterion

$$\bar{\bar{\phi}}(\boldsymbol{t}, \bar{\bar{q}}) = |t_m| - \left(\tau_u - \bar{\bar{q}}\right) \leq 0, \tag{100}$$

and the stress like softening variable

$$\bar{\bar{q}} = \max\left[\tau_u, -K_s \bar{\bar{\xi}}\right], \tag{101}$$

where $K_s = -400$ kN/cm^3. In our simulations we only consider constant jumps in the tangential direction. We assumed that there is a small imperfection in the metal strip, which one can interpret as the starting point of the discontinuity (see Figure 24). Several simulations were made with different mesh sizes ranging from 6 to 384 finite elements. The sum of reaction forces at the right edge versus imposed displacement diagrams are presented in Figure 26. One can see that the mesh size has very little influence on the results. All the curves have three

distinguished phases, namely the linear elastic phase, which is followed by the isotropic hardening phase and the final softening phase. Figure 27 depicts the discontinuity paths for different meshes. In Figure 28 we present deformed configurations (scaled 10 times) for different meshes.

5 Conclusions

A planar finite element with embedded strong discontinuity in displacements has been derived and used to model the fracture process in concrete solids, the delamination in composite materials and the failure in ductile materials. The key feature of the derived element is that it linearly interpolates the displacements jumps in both normal and tangential directions of the discontinuity line. Simple tests show that there is no transition of spurious stresses across the discontinuity line for basic (constant and linear) separation modes. The element is effective for the implementation, since the displacement-jump-parameters are condensed on the element level. However, in order to make the discontinuity propagation algorithm more robust, the continuity of the discontinuity line between the elements is enforced.

References

[1] A. Ibrahimbegovic, Nonlinear Solid Mechanics: Theoretical Formulations and Finite Element Solution Methods, Springer, 2009.

[2] A. Ibrahimbegovic, D. Brancherie, Combined hardening and softening constitutive model of plasticity: precursor to shear slip line failure, Comput. Mech., 31, 88-100, 2003.

[3] B. Brank, D. Perić, F.B. Damjanić, On large deformations of thin elastoplastic shells: Implementation of a finite rotation model for quadrilateral shell element, Int. J. Numer. Meth. Engng., 40, 689-726, 1997.

[4] A. Ibrahimbegovic, F. Gharzeddine, L. Chorfi, Classical plasticity and viscoplasticity models reformulated: Theoretical basis and numerical implementation, Int. J. Numer. Meth. Engng., 42, 1499-1535, 1998.

[5] J.C. Simo, T.J.R. Hughes, Computational inelasticity, Springer, 1998.

[6] J. Dujc, B. Brank, On stress resultant plasticity and viscoplasticity for metal plates, Finite Elements in Analysis and Design, 44, 174-185, 2008.

[7] J. Korelc, AceGen, AceFem, available at http://www.fgg.uni-lj.si/Symech.

[8] C. Linder, F. Armero, Finite elements with embedded strong discontinuities for the modeling of failure in solids, Int. J. Numer. Meth. Engng., 72, 1391-1433, 2007.

[9] J. Mosler, On the modeling of highly localized deformations induced by material failure: the strong discontinuity approach, Arch. Comput. Meth. Engng, 11, 389-446, 2004.

[10] J. Oliver , A.E. Huespe, S. Blanco, D.L. Linero, Stability and robustness issues in numerical modeling of material failure with the strong discontinuity approach, Comput. Methods Appl. Mech. Engrg., 195, 7093-7114, 2006.

[11] O.L. Manzoli, P.B. Shing, A general technique to embed non-uniform discontinuities into standard solid finite elements, Computers and Structures, 84, 742–757, 2006.

[12] J. Dujc, B. Brank, A. Ibrahimbegovic, Multi-scale computational model for failure analysis of metal frames that includes softening and local buckling, Comput. Methods Appl. Mech. Engrg., 199, 1371–1385, 2010.

[13] F. Armero, D. Ehrlich, An analysis of strain localization and wave propagation in plastic models of beams at failure, Comput. Methods Appl. Mech. Engrg. 193, 3129–3171, 2004.

[14] M. Jirasek, Comparative study on finite elements with embedded discontinuities, Comput. Methods Appl. Mech. Engrg. 188, 307–330, 2000.

[15] A. Ibrahimbegovic, E.L. Wilson, A modified method of incompatible modes, Communications in Numerical Methods in Engineering, 7, 187-194, 1991.

[16] J. Mosler, On advanced solution strategies to overcome locking effects in strong discontinuity approaches, Int. J. Numer. Meth. Eng., 63, 1313-1341, 2005.
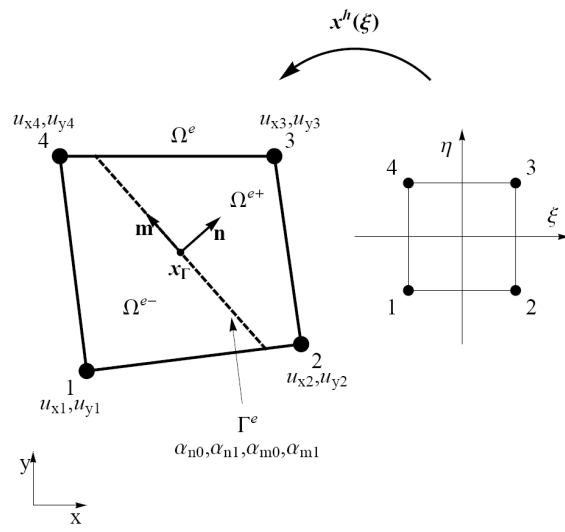
Figure 1: Quadrilateral finite element with embedded discontinuity
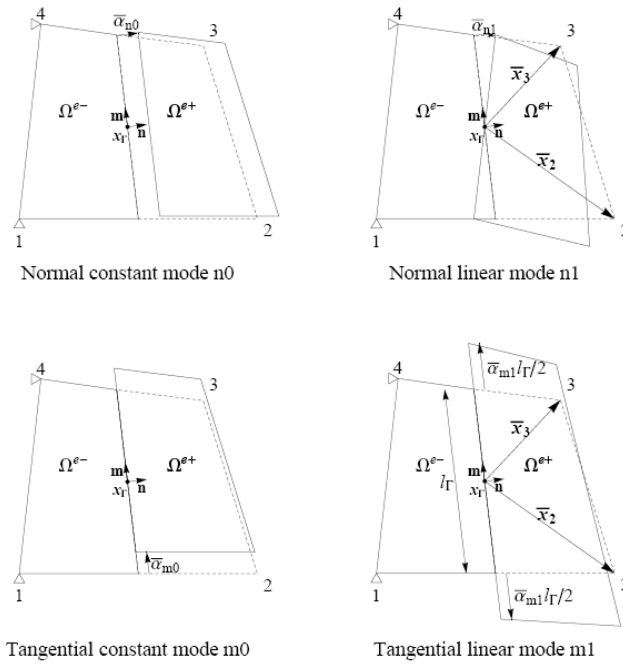
Figure 2: Element separation modes along the discontinuity line
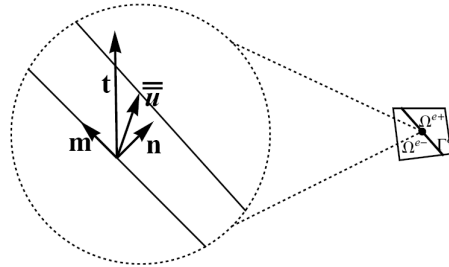
Figure 3: Neighborhood of a point of interest at the discontinuity line Γ^e
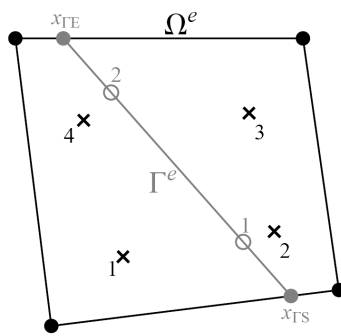
Figure 4: Numerical integration scheme
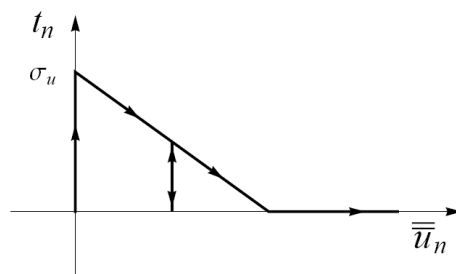
Figure 5: Plastic cohesive law with linear softening in tension
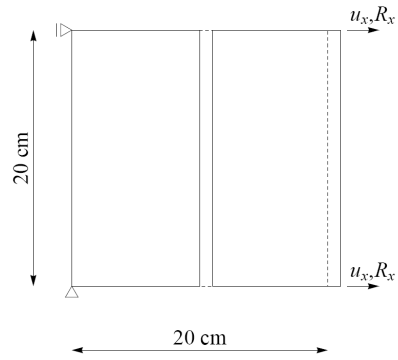
Figure 6: Tension test on a square block
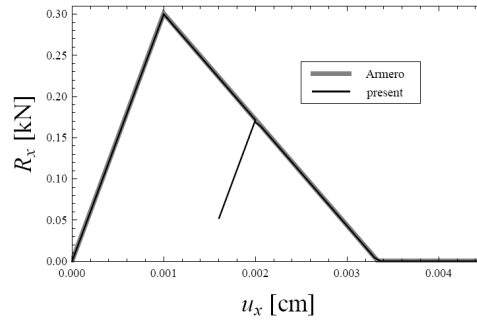
Figure 7: Reaction force versus imposed displacement curves
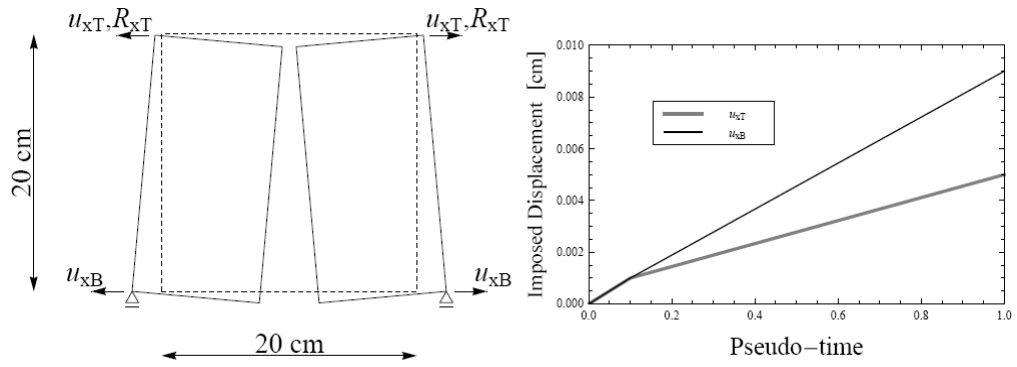
Figure 8: Geometry of the bending test of a square block (left). Imposed displacement versus pseudo-time curves (right).
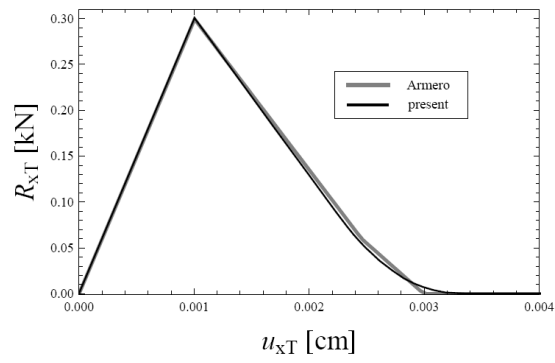
Figure 9: Top reaction force versus imposed top displacement curves
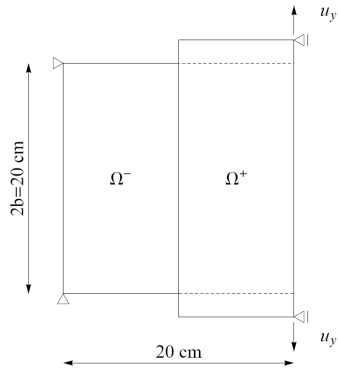
Figure 10: Partial tension test of a square block
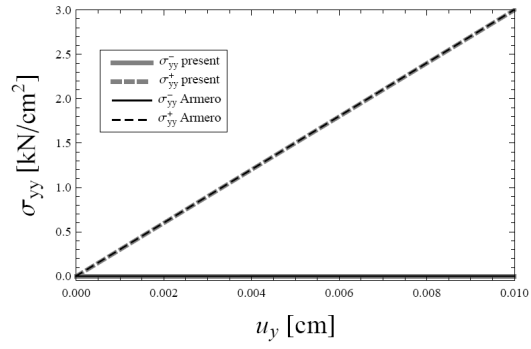
Figure 11: Stress at integration points in Ω^+ and Ω^- region versus imposed displacement curves
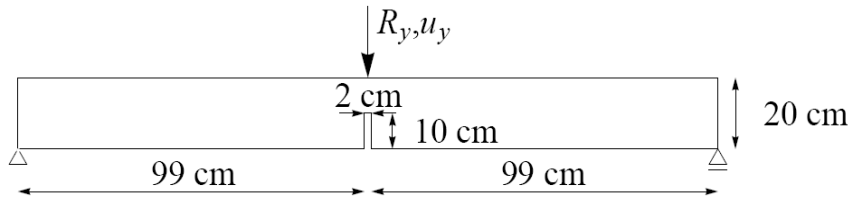
Figure 12: The three point bending test of a notched concrete beam
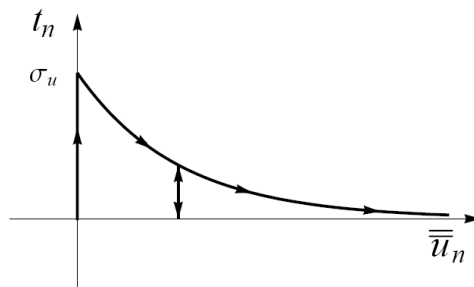
Figure 13: Plastic cohesive law with exponential softening in tension
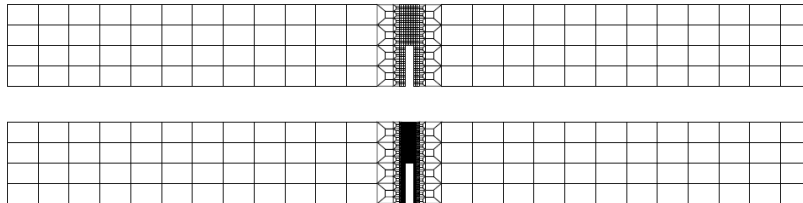
Figure 14: Coarse (top) and fine (bottom) finite element meshes for the three point bending test
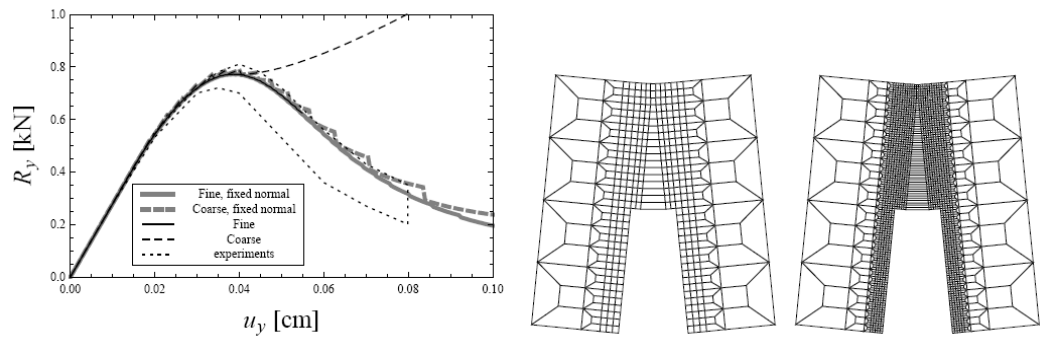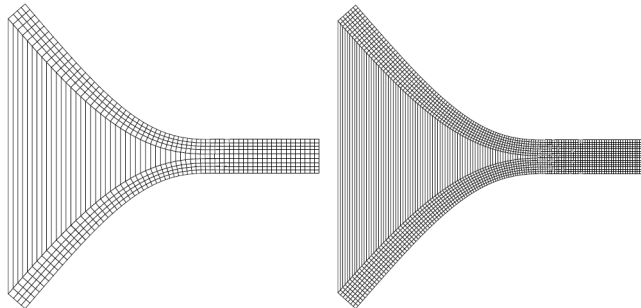
Figure 15: Reaction force versus imposed displacement curves and scaled (100 times) deformed meshes
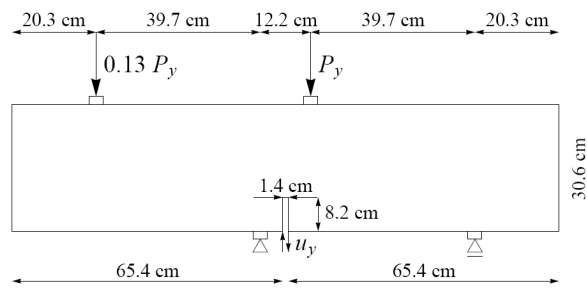
Figure 16: The four point bending test
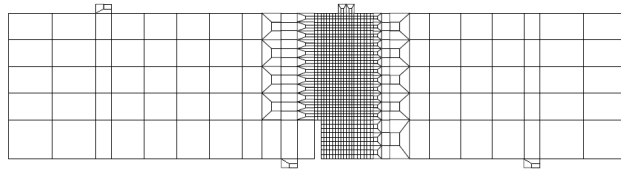
Figure 17: Finite element mesh for the four point bending test
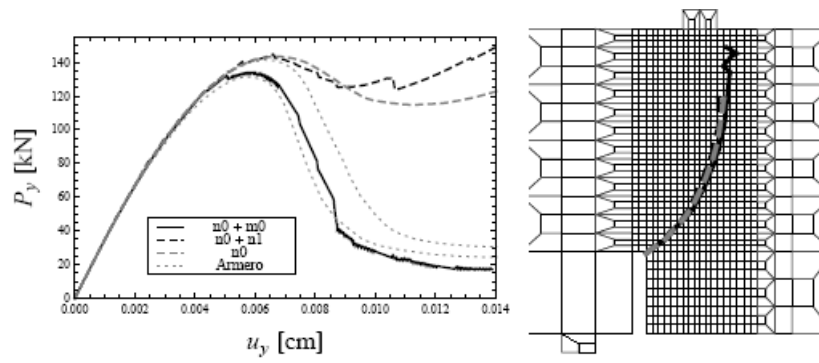
Figure 18: Load versus crack mouth sliding displacement curves and the corresponding crack paths
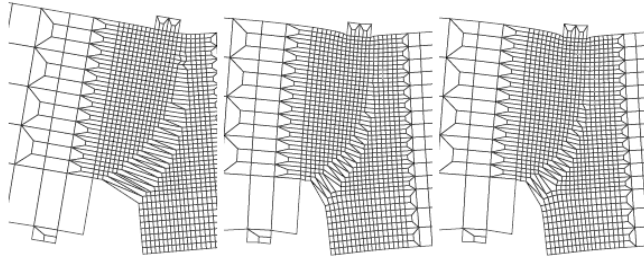
Figure 19: Scaled deformed meshes: the "n0 + m0" (left), the "n0 + n1" (middle) and the "n0" formulations
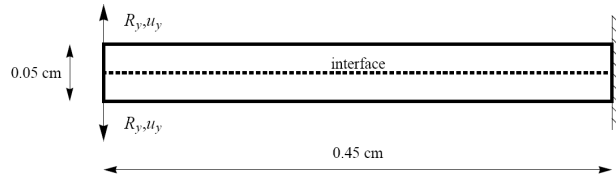
Figure 20: Delamination test data
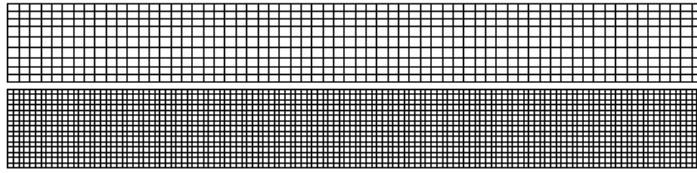
Figure 21: Coarse (top) and fine (bottom) finite element meshes for the delamination test
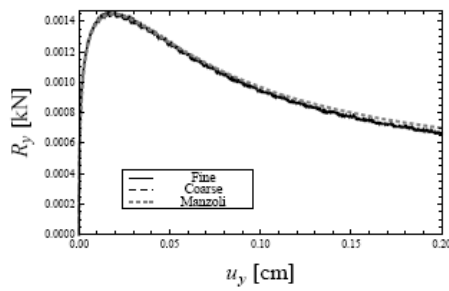
Figure 22: Reaction force versus imposed displacement diagram

Figure 23: Deformed configurations: the coarse mesh (left) and the fine mesh (right)
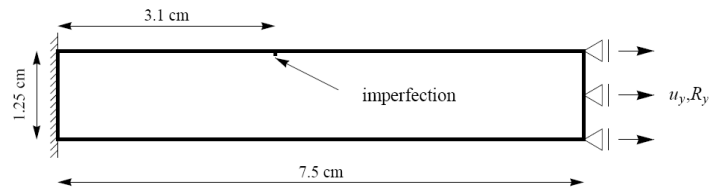
Figure 24: Tension test of a metal strip
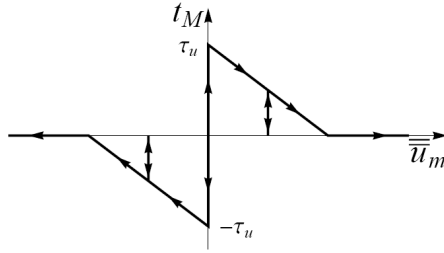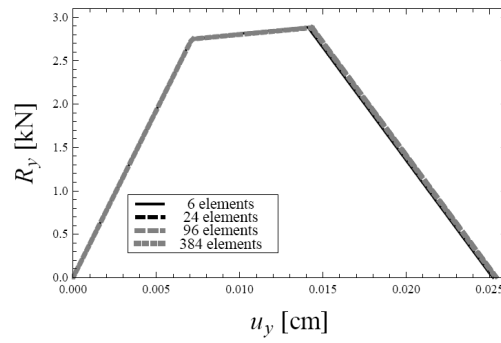
Figure 25: Plastic cohesive law with linear softening

Figure 26: Total reaction force versus imposed displacement curves
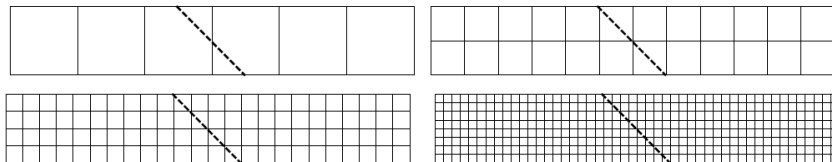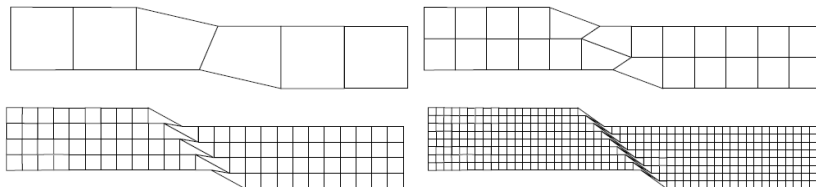

Figure 27: Discontinuity path for several meshes

Figure 28: Scaled deformed configurations